

運用最大概似估計及期望最大演算法以重建與切割微正子斷層掃描與
微陣列影像之統計應用

Statistical Applications of Maximized Likelihood Estimates with the
Expectation-Maximization Algorithms for Reconstruction and Segmentation
of MicroPET and Spotted Microarray Images

研究生：陳泰賓

Student : Tai Been Chen

指導教授：盧鴻興

Advisor : Henry Horng-Shing Lu



博士論文

A Thesis

Submitted to Institute of Statistics

National Chiao Tung University in Partial Fulfillment of the Requirements
for the Degree of Ph. D in Statistics

March 2007

Hsinchu, Taiwan, Republic of China

中華民國九十六年三月

運用最大概似估計及期望最大演算法以重建與切割微正子斷層掃描與微陣列影
像之統計應用

學生：陳泰賓

指導教授：盧鴻興

國立交通大學統計學研究所 博士班

摘 要

正子斷層掃描影像(PET)針對功能性疾病診斷提供非侵入式且可量化等資訊；然而PET影像品質與使用的重建演算法有很高的相依性。屬疊代法之最大概似期望最大法(MLEEM)正快速成為PET影像重建的標準方法。常見的MLEM演算法對於隨機事件修正是採用二個Poisson分配相減(即: Prompt與delay資料相減)，此方法將失去Poisson分配的特性。我們將提出可行的演算法解決此一問題。利用聯合Poisson分配(即聯合Prompt與delay)做隨機事件修正並同時重建PET影像，稱之為PDEM演算法；不僅保持了Poisson分配特性而且不會增加估計隨機事件修正後的變異。利用模擬、實驗假體以及實際老鼠等資料，採用變異係數和半高全寬值比較FBP, OSEM以及PDEM之影像重建品質。經由PDEM所得的影像品質均優於FBP或OSEM。

三維microPET影像能對體內基因反應之追蹤與辨認提供重要的訊息。為了能調查或了解基因表現情形，發展低雜訊且高精確度的重建方法有其必要性。因採用PDEM演算法重建影像接著將利用統計混合模型切割影像。在這研究中，模擬與實際老鼠資料評估所提之方法，結果顯示是所提出的方法具有合理且正確性。

另一應用是對微陣列針狀基因影像之切割；該影像能提生物醫學之基因資訊。在這一應用使用高斯混合模型以及無母數的核密度估計等方法用來切割雙色微陣列針狀基因影像。16片雙色基因影像設計嵌入已知濃度之 spike spots、重複 Spots 以及染劑互換等實驗，將用以驗證與評估所提方法之有效性與正確性；結果顯示所提之方法不僅能有效切割 Spots 同時對 Spots 的估計具有高準確性。

Statistical Applications of Maximized Likelihood Estimates with the
Expectation-Maximization Algorithms for Reconstruction and Segmentation of
MicroPET and Spotted Microarray Images

Student: Tai Been Chen

Advisor : Henry Horng-Shing Lu

Institute of Statistics
National Chiao Tung University

ABSTRACT

Positron emission tomography (PET) can provide *in vivo*, quantitative and functional information for the diagnosis of functional diseases; however, PET image quality is highly dependent on a reconstruction algorithm. Iterative algorithms, such as the maximum likelihood expectation-maximization (MLEM) algorithm, are rapidly becoming the standards for image reconstruction in emission tomography. The conventional MLEM algorithm utilized the Poisson model, which is no longer valid for delay-subtraction after random correction. This study was undertaken to overcome this problem. The MLEM algorithm is adopted and modified to reconstruct microPET images with random correction from the joint Poisson model of prompt and delay sinograms; this reconstruction method is called PDEM. The proposed joint Poisson model preserves Poisson properties without increasing the variances of estimates associated with random correction. The coefficients of variation (CV) and full width at half-maximum (FWHM) values were utilized to compare the quality of reconstructed microPET images of physical phantoms acquired by filtered backprojection (FBP), ordered subsets expectation-maximization (OSEM) and PDEM approaches. Experimental and simulated results demonstrated that the proposed PDEM method yielded better image quality results than the FBP and OSEM approaches.

The segmentation of 3D microPET image is one of the most important issues in tracing and recognizing the gene activity *in vivo*. In order to discover and recover the activity of gene expression, reconstruction techniques with higher precision and fewer artifacts are necessary. To improve the resolution on microPET images, the PDEM method is applied. In addition, the advanced statistical technique based on the mixture model is developed to segment the reconstructed images. In this study, the new proposed method is evaluated with simulation and empirical studies. The performance shows that the proposed method is promising in practice.

The segmentation of cDNA microarray spots is essential in analyzing the intensities of microarray images for biological and medical investigations. In this work, the nonparametric method of kernel density estimation is applied to segment two-channel cDNA microarray images. This approach successfully groups pixels into foreground and background. The segmentation performance of this model is tested and evaluated by sixteen microarrays. Specifically, spike genes with various levels of contents are spotted in a microarray to examine and evaluate the accuracy of the segmentation results. Duplicated design is implemented to evaluate the accuracy of the model. Swapped experiments of microarray dyes are also implemented. Results of this study demonstrate that this method can cluster pixels and estimate statistics regarding spots with high accuracy.

誌 謝

感謝指導老師盧鴻興教授對我的用心教誨、鼓勵與支持，才能使這本論文順利完成！同時也感謝陽明大學陳志成教授與中研院統計所陳珍信教授等人對研究資料提供與研究方法建議，讓本文能有進展。感謝交大統計所有老師的教導；學長姐等人的研究素材與努力；對於我在交大統計求學期間都有著莫大的影響與幫助。

太多人對我求學過程中有情有義；好友一鳴、駿逸、炳熏、棟鴻、紹志，以及沒有登錄的諸位好友們！謝謝你們的鼓勵和打氣，使我得以完成這本論文；同時亦感謝交大管科博士班羅偉給予我實質支持與建言。你們都是我生命中之貴人。



感謝家人對我求學期間的百分百支持；父母兄弟妹給予我勇氣完成此一論文。最後我要謝謝我妻子 雯玲 在我求學與研究期間，不止給我勇氣和鼓勵，亦盡心盡力操持分擔家務同時照顧幼女亭妤；她總是默默付出且靜靜等待，始終對我有信心！本書付印之前，正逢雯玲懷胎 8 個月。謝謝妳的付出與努力，我於此刻以此書，表達我對妳的感恩與謝意。期望我們未來都能平安與健康！

陳泰賓 筆于風城

2007. 04

Contents

中文摘要.....	i
英文摘要.....	ii
誌謝.....	iii
Contents.....	iv
Table Contents.....	v
Figure Contents.....	vi
1. Introduction	1
2. Methodologies	7
2.1 Reconstruction with Random Correction for MicroPET Images	
2.2 Segmentation of 3D MicroPET Images	
2.3 Segmentation of Microarray Images	
3. Applications on MicroPET Images	22
3.1 The MicroPET Scanner	
3.2 Reconstruction with Random Correction	
3.2.1 Simulation Study	
3.2.2 Phantom Study	
3.2.3 Real Mouse Study	
3.3 Segmentation of 3D MicroPET Images	
3.3.1 3D Images	
3.3.2 Simulation Study	
3.3.3 Real Mouse Study	
4. Applications on Microarray Images	42
4.1 The Spotted Microarray Images	
4.2 Evaluation from Spike Genes	
4.3 Evaluation from Duplicated Genes and Swapped Arrays	
5. Discussion and Conclusion	51
6. Future Works	55
7. Acknowledgements	57
8. References	58
9. Appendix	66



Table Contents

Table 2.3.4-1: One set of eight spike genes with target contents and ratios in real microarrays.

Table 2.3.4-2: Another set of eight spike genes with target contents and ratios in real microarrays.

Table 3.2.2-1: Average and standard deviation (in mm) of 28 FWHMs for horizontal and vertical line profiles measured for comparing the spatial resolutions of PDEM, OSEM and FBP. Those values are measured at the 31st slice.

Table 3.2.2-2: A circular ROI with a radius of 9 pixels to the center of the uniform phantom was utilized to compare noise levels between the PDEM, FBP and OSEM. Those values were measured at the 40th reconstructed slice.

Table 3.3.2-1: Comparisons of the clustering results by K-means and GMM in Fig. 3.3.2-1A.

Table 3.3.3-1: The FWHMs and SNRs of segmented results by GMM are better than those by K-means in Fig. 3.3.3-5.

Table 4.2-1: The comparisons of SSEs are obtained for different methods based on spike genes. Array 1s is that obtained by swapping the dyes of Array 1. Relative improvement is specified by $(GenePix-Method)/GenePix$ as a percentage.

Table 4.2-2: The comparisons of SSREs are obtained for different methods based on spike genes.. Array 1s is that obtained by swapping the dyes of Array 1. Relative improvement is specified by $(GenePix-Method)/GenePix$ as the percentage.

Table 4.3-1: Used spots excluding spike spots and bad spots in each array are listed and “x2” means two duplicates on every array.

Figure Contents

Fig. 2.2.1-1. An example shows the procedure to decide the number of clusters and initialized values in the EM algorithm of GMM. There are two peaks from the estimated densities of $\hat{f}(y)$. Hence, the number of clusters in GMM will be two and initialized values will be computed from the above equations.

Fig. 3.1-1: The microPET R4 scanner in Taipei Veterans General Hospital is displayed.

Fig. 3.1-2: Two images of microPET sinograms from physical experiments of six point sources are displayed. In every sinogram, the horizontal axis represents the ordering of line of responses (LORs) and the vertical axis represents different angles from 0 degree to 180 degree. The pixel intensity in the sinogram records total gamma rays detected in a scanning time window.

Fig. 3.1-3: The above data matrices are used for reconstruction by the PDEM and segmentation by the GMM.



Fig. 3.1-4 The above data matrices are used for reconstruction by the FBP and OSEM with random pre-correction.

Fig. 3.2.1-1. The modified Shepp-Logan head image was used for simulation studies. The line profiles of PDEM were less noisy than those of FBP and OSEM. The PDEM technique reconstructed better images than the FBP and OSEM did with 5%, 10% and 30% random noise. All images were rescaled using their own maximum values.

Fig. 3.2.2-1. The 31st slice of the 28 line-source phantom reconstructed using the three methods are displayed. Both FBP and OSEM are reconstruction methods built into the microPET R4 system. All images were rescaled using their own maximum values. The images are shown in the rectangular window. Table 3.2.2-1 presents the comparisons of their FWHMs.

Fig. 3.2.2-2. The reconstructed 40th slice from a uniform phantom was used to investigate noise level generated by the three approaches. The white line indicates the position of the investigated line profile. All images were rescaled using their own maximum values. The images are shown in the rectangular window with enlarged central parts. Table 3.2.2-2 presents the comparisons of their CVs.

Fig. 3.2.3-1: Sagittal (top) and coronal (middle) images of the first mouse image reconstructed by PDEM (left), FBP (middle) and OSEM (right). The images reconstructed by PDEM have less noise than those reconstructed using FBP and OSEM with comparison by line profiles. The images are shown in the rectangular window with enlarged central parts.

Fig. 3.2.3-2. Coronal and sagittal images of the second mouse image reconstructed using PDEM (left), FBP (middle) and OSEM (right). The images reconstructed by PDEM have less noise than those reconstructed by FBP and OSEM, as shown in the respective line profile near the heart. The images are shown in the rectangular window with enlarged central parts.

Fig. 3.3.1-1. The flow chart of 3D segmentation is plotted.

Figure 3.3.1-2: 3D microPET images for 63 slices are illustrated. Every image has the pixels size of 128 by 128.

Fig. 3.3.2-1. **A)** Simulation image of five clusters is displayed. **B)** Adding 50% noise into panel A. **C)** Clustering results using GMM. **D)** Kernel density curve using **C** with values of high and low peaks. Four peaks are identified on the density curve. Hence, the number of groups is set as four.

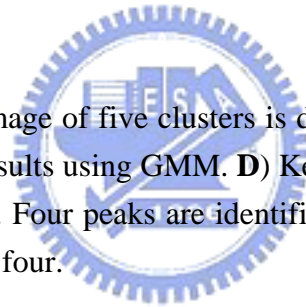


Fig. 3.3.2-2. Target ROIs are marked.

Fig. 3.3.2-3. The results of **A)** by K-means and **B)** by GMM clustering are shown.

Fig. 3.3.2-4. Simulated volume data including slice 1 and 2 are marked as **A** and **B**. **C** and **D** are reconstructed images after added 50% noise ratio to **A** and **B**. **E** and **F** are segmented results without slice normalization. **G** and **H** are segmented results with slice normalization. **I** is the estimated kernel density curve of simulated volume data after slice normalization.

Fig.3.3.3-1. The estimated kernel density curve using the rat volume data of 10 slices is shown with values of high and low peaks. There are four peaks. Hence, the number of groups is set as four. Values of peaks are applied to compute the starting values in EM algorithm.

Fig. 3.3.3-2. The reconstructed rat images are shown from the 51st (top-left) to the 60th (bottom -right) slice.

Fig. 3.3.3-3. The results of segmentation by the GMM are shown from the 51st (top-left) to the 60th (bottom -right) slice.

Fig. 3.3.3-4. The results of segmentation by the K-means are shown from the 51st (top-left) to the 60th (bottom -right) slice.

Fig. 3.3.3-5. The horizontal line profile of the 60th slice of Fig. 3.3.3-2 is shown with FWHMs. The FWHMs of region 1, 2, 3 and 4 are 3.75, 3.40, 4.14 and 4.45 pixels respectively. The top part shows the location of this line profile in the MLEM reconstruction image and the segmentation by GMM and K-means.

Fig. 4.1-1: An example of microarray image with 32 blocks, 22 columns and 22 rows. One block is enlarged and eight spike genes are numbered.

Fig. 4.1-2: Typical segmentation of two spot images by the irregular segmentation method of GenePix 6.0. Parts a) and b) present the original images of Cy5 and Cy3 dyes. Parts c) and d) present the segmented region on the images of Cy5 and Cy3 dyes.

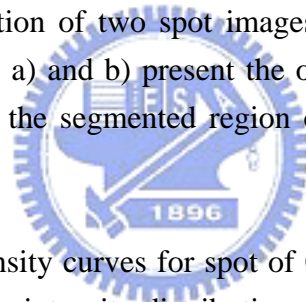


Fig. 4.1-3: Two estimated density curves for spot of Cy5 (a) and Cy3 (b) dyes. Both Cy3 and Cy5 images have two intensity distributions for background and foreground pixels. The local minimum is used to be cutting point for segmenting spot pixels.

Fig. 4.3-1: Top row shows four methods to evaluate duplicated spots for 3rd (red) and swapped 3rd (blue) arrays. The x-axis and y-axis represent average and difference between duplicated spots. Bottom row shows four methods to evaluate swapped arrays (3rd, 3rd s). The x-axis and y-axis represent summation and difference between swapped arrays.

Figure 4.3-2 shows the concordance correlation coefficients, Pearson's correlations and standard deviations between replicates gene expression of sixteen arrays and eight swapped arrays.

Fig. 4.3-2: Top and down figure are concordance correlations, Pearson's correlations and standard deviations between duplicated spots of sixteen arrays and between swapped arrays of eight arrays using the GKDE, KDE, GMM and GenePix 6.

Fig. B-1: The illustration of HWHM is shown.

Fig. B-2: The true, random, and scatter coincidence events are illustrated.



1. Introduction

The techniques of microPET and microarray are two of the most powerful modalities in the study of molecular gene therapy and gene expression profiles in this century.

The high spatial resolution and sensitivity of microPET make it an ideal modality for *in vivo* gene imaging. Those images can be employed to monitor the effects of gene therapy inside animal bodies. Recent study [1] shows that the technique of microPET has been developed to trace the gene expression *in vivo*. Hence, it is very important to enhance the reconstruction and analysis techniques with better precision and fewer artifacts so that the genuine gene expression inside biological objects can be recovered. High-quality image reconstruction is essential in establishing a solid basis for quantitative study of microPET images [2-3].

The conventional methods built-in microPET software (microPET manager V1.6.4), filter backpropagation (FBP) [4] and ordered subsets expectation-maximization approach (OSEM) [5], are used to reconstruct microPET images after applying the Fourier rebinning (FORE) algorithm [6] and random pre-correction. However, the FBP is unable to model the randomness of PET. As the FBP was developed for transmission tomography, it is not accurate when applied to emission tomography which contains randomness in PET. Hence, the FBP reconstruction of microPET

image is typically noisy and inaccurate. Meanwhile, the OSEM can reconstruct more accurate images than the FBP does, but it is basically driven from the inaccurate Poisson model using random pre-correction (that is, applying subtraction on two random variables from two independent Poisson distributions).

On the contrary, iterative algorithms, such as the maximum likelihood expectation-maximization (MLEM) algorithm, are rapidly becoming the standards for image reconstruction in emission tomography. The MLEM reconstruction and related improvements have also been reported in literature [7-10, 14, 16-17, 21-24]. Statistical analysis that supports positron emission tomography (PET) has been discussed as well [9]. The MLEM approach can model randomness in emission tomography with the asymptotic efficiency by applying the row operation and monotonic convergence using the EM algorithm. Furthermore, the EM algorithm can be parallelizable for 3D PET image reconstruction [10].

The generation of quantitative PET images requires that the effects of random coincidences and coincidence efficiencies are corrected [11-12]. One random correction approach applies single count rates to a prompt sinogram [13]. This approach is generally based on geometric and physical characteristics. However, this approach makes many assumptions for approximations that can decrease the accuracy of random correction below that obtained using methods that utilize both prompt and

delay sinograms. An alternate approach applies random pre-correction to sinograms by subtracting the delay sinogram from a prompt sinogram before the processing of images reconstruction. The random pre-correction using various approximations has been applied to correct random (or accidental) coincidental events [14-15]. Different methods have been developed to approximate the distribution of random pre-correction [16-18]. However, random pre-correction increases the variances of estimates [17, 19]. Since the distribution of random pre-correction is no longer Poisson-distributed, the shifted Poisson methods and saddle-point (SD) approximation have been generated to enhance approximation [20]. This study proposes a joint Poisson model of prompt and delay sinograms for random correction with the MLEM reconstruction without using approximations nor increasing variances. This approach is named PDEM. Simulations, physical phantoms and real Mouse studies of the PDEM method using the microPET R4 system were performed. This study analyzed and assessed the reconstruction of 2D data obtained from 3D sinograms after applying the FORE method to verify the proposed approach. The PDEM method can also be utilized in future studies reconstructing 3D images.

Once microPET images have been reconstructed using PDEM, the next step is to segment those regions of interest (ROI) from the reconstructed images. The FBP reconstruction has been applied in tomography due to its power of fast computation.

Wong *et al.* [26-28] used the method of FBP reconstruction and K-means clustering with Akaike information criterion (AIC) [25] to segment PET images. However, the FBP method is not accurate for reconstructing microPET images. Hence, the PDEM is applied to reconstruct microPET images more accurately instead of the FBP in this study. Due to the variability of variances among different segments of microPET images, we will consider the Gaussian mixture model (GMM) instead of K-means clustering [28-30]. Furthermore, the numbers of cluster and their initialized values used in GMM are determined by the kernel density estimation (KDE).

Similar methods can be adapt to segment spotted microarray images. The microarray is a high throughput technique for exploring the expression profiles for thousands of genes during the studies of genomics in biology and medicine. Although high-density oligonucleotide arrays are currently available, custom-made or spotted cDNA microarrays have also been used, because of their favorable cost, ease of preparation and ease of analysis in the design of co-hybridization experiments [32]. Studies of the functionality of genes in this new era of post-genomics are important [33]. Analyzing the microarray images with high accuracy is essential to measure the gene expression profiles. Advanced analysis for selecting significant genes, clustering, classification, and network reconstruction of gene expression profiles can proceed on a solid foundation following complete accurate measurements [34-35].

The cDNA images, in general, tend to be very noisy. Therefore, various approaches have been proposed to improve the calibration of scanning efficiencies, the alignment and detection of spotting errors, the denoising of background noise from images, the marking of dust, gridding, moving, hybridization and other artifacts [34, 36-37]. Different methods have been proposed for segmenting cDNA microarray images in literature. Markov Random Field (MRF) modeling has been proposed to segment spots in microarray images [32]. This MRF-based approach relies on the prior assumption of class labeling of all pixels [38] and it has a high computational cost. The alternative approach of region-growing approach relies on the selection of initial seeds that influence its performance [39]. The other approach of Gaussian mixture model (GMM) generally assumed normality when it is applied to this segmentation problem [40]. Accordingly, this study is motivated by the need to investigate the segmentation of cDNA microarray images using the nonparametric method of kernel density estimation (KDE) that does not require the assumption of normality.

In this investigation, the KDE is utilized to classify pixels in a spot into background and foreground that use the estimated density to find the cut-off value. Meanwhile, the approach of initial segmentation using GMM and fine tuning using KDE is proposed to detect feasible boundary between foreground and background in spots. This approach is named GKDE (that is, GMM + KDE). Empirical studies are

conducted on real microarray data that involve 256 spike genes with known contents.

The segmentation results obtained by the KDE are compared with those obtained using the adaptive irregular segmentation method used in the current version of GenePix Pro software 6.0 (at http://www.moleculardevices.com/pages/software/gn_genepix_pro.html, with the accompanying User's Manual).

Microarrays with various sources and experimental designs are needed to monitor the variations of gene expressions. Spike spots of the corresponding spike mRNAs with a range of concentrations are used to monitor the variability of fluorescence intensities and determine the consistency of hybridization among arrays. The spike spots also reveal the variations of pins in an array. Duplicated spots within each array are used to assay the hybridization process of the arrays. Swapped experiments are also used to assay the labeling efficiency of Cy3 and Cy5 fluorescence dyes.

In this application, real microarray images with (1) spike spots with various ratios of Cy5 to Cy3 intensities, (2) duplicated spots in an array and (3) the swapping of microarray experiments, are applied to evaluate the performance and accuracy of the segmentation method.

2. Methodologies

This chapter begins with the introduction of algorithms and methods used for reconstruction and segmentation accordingly. Section 2.1 introduces the proposed PDEM approach to reconstruct microPET images with random correction. Section 2.2 shows the GMM applied to segment 3D microPET images by the automatic determination of the number of clusters and initialized values by KDE. Section 2.3 presents the GKDE approach that is applied to segment spotted cDNA microarrays.

2.1 Reconstruction with Random Correction for MicroPET Images

A new approach is proposed to reconstruct microPET images with random correction by the joint Poisson model of prompt and delay sinograms. We will assume that the data in prompt and delay sinograms follow two independent Poisson distributions that are labeled as (1) and (2).

$$n_p^*(d) \sim \text{Poisson}(\lambda^*(d)), \quad (1)$$

$$n_d^*(d) \sim \text{Poisson}(\lambda_r^*(d)), \quad (2)$$

where $\lambda^*(d) = \lambda_l^*(d) + \lambda_r^*(d) = \sum_b P(b,d)\lambda_l(b) + \lambda_r^*(d)$, b indicates the b^{th} pixel of a target image with size $B = 128 \times 128$ in which $b=1,2,\dots,B$, and d indicates the d^{th} LOR with total numbers $D = 96 \times 84$ in which $d=1,2,\dots,D$. The term $n_p^*(d)$ is the number of coincidental events in the prompt sinogram at the d^{th} projection line of response (LOR), which is formed by two detectors with the Poisson mean, $\lambda^*(d)$; $n_d^*(d)$ is the

number of random coincidental events in the delay sinogram with the Poisson mean $\lambda_r^*(d)$; $P(b,d)$ is the system probability matrix from the b^{th} pixel to the d^{th} LOR. Parameters of $\lambda_t(b)$ and $\lambda_r^*(d)$ are unknown and must be estimated. Parameter $\lambda_t(b)$ represents the intensities of true coincidental events. Appendix (A3) lists the log-likelihood of observed data in the prompt and delay sinograms. Since the maximum likelihood estimate (MLE) is difficult to find by maximizing Eqs. (1) and (2) numerically, the EM algorithm [30-31] can be utilized (as the details in Appendix). Equations (3) and (4) are the i^{th} iteration steps of the PDEM.

$$\lambda_t^i(b) = \frac{\lambda_t^{i-1}(b) \sum_{d=1}^D n_p^*(d) p(b,d)}{\sum_{d=1}^D P(b,d) \sum_{b'=1}^B p(b',d) \lambda_t^{i-1}(b') + \lambda_r^{*i-1}(d)}, \quad (3)$$

$$\lambda_r^{*i}(d) = \frac{1}{2} \left[\frac{n_p^*(d) \lambda_r^{*i-1}(d)}{\sum_{b'=1}^B p(b',d) \lambda_t^{i-1}(b') + \lambda_r^{*i-1}(d)} + n_d^*(d) \right], \quad (4)$$

where $i=1,2,\dots,I$, is the number of iterations.

The MLEM algorithm of joint the prompt and delay sinograms is described as follows and such a scheme is called PDEM reconstruction.

Algorithm for PDEM reconstruction:

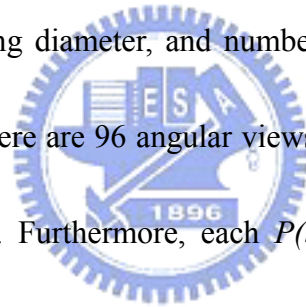
Step 1: Set the initial parameters ($i=0$) using the FBP, the method of moments estimate (MME) or alternative approaches.

Step 2: The iteration number is increased by 1 (that is, i is replaced by $i+1$). Update

the parameters by applying Eqs. (3) and (4).

Step 3: If $l_{in}(\lambda_t^i(b), \lambda_r^{*i}(d)) - l_{in}(\lambda_t^{i-1}(b), \lambda_r^{*i-1}(d)) < tolerance$ (that is, the difference of log-likelihoods among new and old estimates is smaller than for a tolerance level), then the iteration is terminated; otherwise, go to Step 2.

This method preserves Poisson properties and update estimates iteratively. In this study, $P(b,d)$ was computed from LORs and the locations of pixels based on the geometric characteristics of the microPET R4, including number of detectors, image size, field of view (FOV), ring diameter, and number of angular views. The matrix size of one slice is 96×84 . There are 96 angular views and 84 LORs for each angular view during image scanning. Furthermore, each $P(b,d)$ can be identified from its detector pairs of LOR and image pixel location. Therefore, the PDEM reconstructs the sinogram after the step that sinograms are rebinned by the FORE approach in the microPET system.



2.2 Segmentation of 3D MicroPET Images

This section briefly introduces the segmentation algorithm of 3D microPET image. Several pre-processing steps are used before the GMM algorithm is applied to segment 3D microPET image. The number of clusters to be used in GMM and the initialized values of each cluster are needed in applying the GMM method. Hence, the

nonparametric method of KDE is employed to estimate the density curve of image intensities. The numbers of cluster (k) can be determined by searching the number of local maximum points from the estimated density curve. In addition, the initialized values of parameters for the normal distributions in k clusters can be determined from the data consequently.

2.2.1 Determination of the Cluster Number for GMM

The kernel density estimation (KDE) [41] will be applied to determine the number of clusters used in GMM. From the estimated density curve, those high and low peaks could be used to estimate the means and standard deviations of Gaussian distributions in clusters. It is based on the empirical rule that the range of $\mu \pm 3\sigma$ covers most of observations from a normal distribution. Hence, the initialized values of GMM are determined by applying this empirical rule (as illustrated in Fig. 2.2.1-1). This approach can automatically decide the cluster number and starting values of parameters in the EM algorithm of GMM. This is a simple and computation efficiently method. The details are reported in the following algorithm.

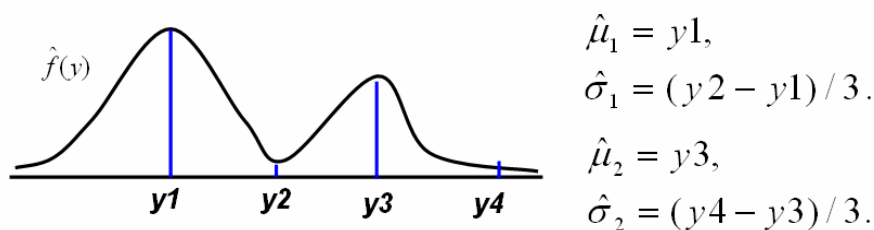


Fig. 2.2.1-1. An example shows the procedure to decide the number of clusters and initialized values in the EM algorithm of GMM. There are two peaks from the estimated densities of $\hat{f}(y)$. Hence, the number of clusters in GMM will be two and initialized values will be computed from the above equations.

Algorithm of KDE for Determining the Number of Clusters

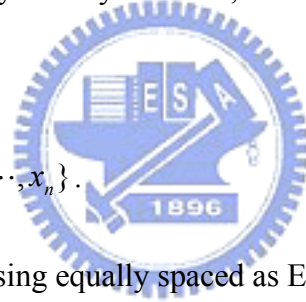
A Gaussian kernel function is used to estimate the density of data as in Eq. (5),

$$\hat{f}(y_j) = \frac{1}{n} \sum_{i=1}^n \frac{1}{\sqrt{2\pi}h} \exp\left(-\left(\frac{y_j - x_i}{h}\right)^2 / 2\right), \quad (5)$$

where x_i is the i^{th} sample, y_j is the j^{th} grid point, h is a bandwidth using in the Gaussian kernel to estimate a probability density function, n is the sample size, and $j = 1, 2, \dots,$

128.

Step 1: Input data $X = \{x_1, x_1, \dots, x_n\}$.



Step 2: Find 128 grid points using equally spaced as Eq. (6):

$$y_j = \text{Min}(X) + j(\text{Max}(X) - \text{Min}(X)) / m. \quad (6)$$

Step 3: Calculate the data-driven bandwidth for KDE as Eq. (7):

$$h = 0.9 \text{Min}\left\{\text{Std}, \frac{\text{IQR}}{1.34}\right\} n^{-1/5} \quad (7)$$

where Std is the standard deviation of X and IQR is the interquartile rang of X

[44].

Step 4: Calculate the KDE using Eq. (5).

Step 5: Determine the number of clusters by counting the number of local maximum.

The high and low peaks of estimated density can be used to estimate the means and

standard deviations of Gaussian distributions in clusters like the illustration in Fig.

2.2.1-1.

2.2.2 Gaussian Mixture Model (GMM)

For the study of a set of 3D images from microPET, I_{xyz} represents the intensity at the xyz^{th} voxel. The range of the position xy in one slice has the size of 128x128 and the number of slices z has the size of 10 in this study. Since the variance scale in different segments of 3D images may be different, we consider Gaussian mixture model with different parameters of means and variances in various clusters [28-29].

We will suppose that the image data I_{xyz} follow a mixture of K distributions with the mixing probability π_k such that

$$\sum_{k=1}^K \pi_k = 1, \text{ and } 0 \leq \pi_k \leq 1 \text{ for all } k = 1, 2, \dots, K. \quad (8)$$

That is, the probability density function of I_{xyz} is

$$f(I_{xyz}; \Phi) = \sum_{k=1}^K \pi_k f_k(I_{xyz}; \theta_k), \quad (9)$$

where $f_k(I_{xyz}, \theta_k)$ refers to the probability density function in the k^{th} cluster with parameter θ_k . All parameters are collected to form a parameter vector $\Phi = (\pi_1, \dots, \pi_K, \theta_1, \dots, \theta_K)$. The MLE of every parameter is usually difficult to obtain directly by numerical methods. Alternatively, the EM algorithm can be applied to find the MLE iteratively [28-29]. Firstly, we introduce an index function as follows,

$$C_{xyzk} = \begin{cases} 1, & \text{if } I_{xyz} \text{ comes from } k^{\text{th}} \text{ normal distribution;} \\ 0, & \text{otherwise.} \end{cases} \quad (10)$$

Let $C_{xyz} = (C_{xyz1}, \dots, C_{xyzK})$ denote the unobserved index vector and $\{I_{xyz}, C_{xyz}\}$ form the complete data for applying the EM algorithm. Given C_{xyz} , the conditional density of I_{xyz} becomes

$$f(I_{xyz} | C_{xyz}) = \sum_{k=1}^K C_{xyzk} \pi_k f_k(I_{xyz}; \theta_k). \quad (11)$$

The EM algorithm finds MLE of parameters with the constraint of Eq. (8) by the following iterative procedure:

$$\omega_{xyzk} = \frac{\pi_k^{(old)} f_k(I_{xyz}; \theta_k^{(old)})}{\sum_{j=1}^K \pi_j^{(old)} f_j(I_{xyz}; \theta_j^{(old)})}, \quad (12)$$

$$\pi_k^{(new)} = \frac{1}{N} \sum_{xyz=1}^N \omega_{xyzk}, \quad (13)$$

$$\mu_k^{(new)} = \frac{\sum_{xyz=1}^N \omega_{xyzk} \cdot I_{xyz}}{N \cdot \pi_k^{(new)}}, \quad (14)$$

$$\sigma_k^{2(new)} = \frac{\sum_{xyz=1}^N \omega_{xyzk} \cdot (I_{xyz} - \mu_k^{(new)})^2}{N \cdot \pi_k^{(new)}}. \quad (15)$$

The Gaussian distribution for the k^{th} cluster is listed below,

$$f_k(x; \theta_k) = f_k(x; \mu_k, \sigma_k) = (2\pi\sigma_k^2)^{-\frac{1}{2}} \exp\left(-\frac{1}{2}(x - \mu_k)^2 / \sigma_k^2\right). \quad (16)$$

The resulting EM algorithm for GMM is described as follows.

EM Algorithm for GMM

Step 1: Set the initial parameters $\Phi^{(old)}$.

Step 2: Update the parameters by using Eqs. (12) - (15).

Step 3: If $l_{in}(\Phi^{(new)}) - l_{in}(\Phi^{(old)}) < tolerance$ (that is, the difference of log-likelihoods among new and old estimates is smaller than for a tolerance level), then the iteration stops. Otherwise, go to Step 2 with the old values of parameters replaced by the new values.

2.2.3 Slice Normalization

The intensity heterogeneity in slices of microPET images comes from the differences in emission activities and reconstruction processes. The heterogeneity between slices will affect the accuracy of the segmentation of 3D images. Hence, slice normalization is needed before 3D segmentation to adjust image levels between slices.

We will use the slice normalization defined in Eq. (17),

$$I_{xyz}^{new} = a \frac{I_{xyz} - Min_z}{Max_z - Min_z}, \quad (17)$$

where I_{xyz}^{new} is the new intensity after slice normalization, I_{xyz} is the original intensity at xyz^{th} voxel, Min_z is the minimum value of the z^{th} slice, Max_z is the maximum value of the z^{th} slice, and a is a nonzero constant for the range of adjusted image level.

2.3 Segmentation of Microarray Images

This section discusses three segmentation algorithms for spotted microarrays. Empirical evaluation of the performance for segmentation methods will use different criteria based on target ratios of spike genes, duplicate spots in a microarray image, and swapped microarray images Cy3 and Cy5 dyes. In this study, the aim is to segment pixels into foreground or background. Hence, there are two clusters used for the segmentation of the pixel intensities in a spot. Besides the GMM with EM algorithm, we will propose the KDE and GMM incorporated the KDE (GKDE) to segment spotted microarray image in this study.

2.3.1 Kernel Density Estimation (KDE)

The KDE with automatic bandwidth selection [41] is used to estimate the density function of pixel intensities for each spot. The Gaussian kernel function and 128 grid points are used for the KDE for each spot as Eq. (5) in section 2.2.1. The details are reported in the following algorithm.

Algorithm for Segmenting One Spot by KDE

Step 1: Input data $X = \{x_1, x_1, \dots, x_n\}$.

Step 2: Find 128 grid points that are equally spaced as Eq. (6).

Step 3: Calculate the data-driven bandwidth for KDE as Eq. (7).

Step 4: Calculate the KDE using Eq. (5).

Step 5: Search the cut-off point (CP) that is the first local minimum of the KDE at y_j^*

and let $CP = y_j^*$.

Step 6: Segment the pixel x_i into foreground if $x_i > CP$, else into background.

2.3.2 Gaussian Mixture Model (GMM)

The GMM assumes that the distribution of foreground intensities is a Gaussian distribution $f_1(\mu_1, \sigma_1^2)$ with mean μ_1 and variance σ_1^2 ; while the distribution of background intensities is another Gaussian distribution $f_2(\mu_2, \sigma_2^2)$ with mean μ_2 and variance σ_2^2 . Hence, the distribution of the intensity at every pixel x_j in a spot can be modeled as a mixture of two Gaussian distributions as Eq. (18).

$$f(x_i; \phi) = \pi_1 f_1(x_i; \mu_1, \sigma_1^2) + \pi_2 f_2(x_i; \mu_2, \sigma_2^2), i = 1, \dots, n, \quad (18)$$

where $f_m(x_i; \mu_m, \sigma_m^2) = \frac{1}{\sqrt{2\pi\sigma_m^2}} \exp\left(-\frac{(x_i - \mu_m)^2}{2\sigma_m^2}\right)$, $m = 1, 2$, $\phi = \{\pi_m, \mu_m, \sigma_m^2, m = 1, 2\}$ and

π_m is the mixing (or prior) probability for the foreground and the background constrained by $0 \leq \pi_m \leq 1$ and $\pi_1 + \pi_2 = 1$. The foreground intensities typically include those of the signals and noise. Therefore, the mean foreground intensity usually exceeds the mean background intensity. Accordingly, the condition $\mu_1 \geq \mu_2$ is considered in this study, which is also commonly used in the literature of normal mixtures [28]. The log-likelihood of the observed data in the model of two mixtures is

Eq. (19).

$$\log(L(\phi | x)) = \sum_{i=1}^n \log\left(\sum_{m=1}^2 \pi_m f_m(x_i; \mu_m, \sigma_m^2)\right). \quad (19)$$

To estimate the above parameters, the EM algorithm can be applied [26]. The segmentation algorithm of one spot using the GMM is listed below.

Algorithm for Segmenting One Spot by GMM

Step 1: Input initial parameters: $k = 0$ and $\phi^{(k)} = \{\pi_m^{(k)}, \mu_m^{(k)}, \sigma_m^{2(k)}, m = 1, 2.\}$. In this

study, the initial parameters are set as follows. Initial μ_1 and μ_2 are set to the first and third quartiles of pixel intensities in one spot. Initial σ_1 and σ_2 are the standard deviations of the pixel intensities below the first quartile and above than the third quartile, respectively. Initial π_1 and π_2 values are set to 0.5.

Step 2: Calculate
$$\tau_{im}^{(k)} = \frac{\pi_m^{(k)} f_m(x_i; \mu_m^{(k)}, \sigma_m^{2(k)})}{\sum_{l=1}^2 \pi_l^{(k)} f_l(x_i; \mu_l^{(k)}, \sigma_l^{2(k)})}.$$

Step 3: Calculate new estimates of

$$\begin{aligned} \phi^{(k+1)} &= \{\pi_m^{(k+1)}, \mu_m^{(k+1)}, \sigma_m^{2(k+1)}, m = 1, 2.\} \\ &= \left\{ \frac{1}{n} \sum_{i=1}^n \tau_{im}^{(k)}, \frac{\sum_{i=1}^n \tau_{im}^{(k)} x_i}{\sum_{i=1}^n \tau_{im}^{(k)}}, \frac{\sum_{i=1}^n \tau_{im}^{(k)} (x_i - \mu_m^{(k+1)})^2}{\sum_{i=1}^n \tau_{im}^{(k)}}, m = 1, 2. \right\}. \end{aligned}$$

Step 4: If $\log(L(\phi^{(k+1)} | x)) - \log(L(\phi^{(k)} | x)) < tolerance$ and the tolerance is set to 10^{-2}

here, then the iteration is terminated. Otherwise, $k \leftarrow k+1$,

$\phi^{(k)} \leftarrow \phi^{(k+1)} = \{\pi_m^{(k+1)}, \mu_m^{(k+1)}, \sigma_m^{2(k+1)}, m = 1, 2.\}$, and the iteration goes to Step 2.

Step 5: Segment the pixel x_i into foreground or background according to the maximum of posterior probabilities with the final values of the parameters,

$$\tau_{im}^{(k+1)} = \frac{\pi_m^{(k+1)} f_m(x_i; \mu_m^{(k+1)}, \sigma_m^{2(k+1)})}{\sum_{l=1}^2 \pi_l^{(k+1)} f_l(x_i; \mu_l^{(k+1)}, \sigma_l^{2(k+1)})}.$$

2.3.3 GMM Incorporated with KDE (GKDE)

We can combine the methods of GMM and KDE, which will be abbreviated as GKDE. The GMM can provide the initial segmentation and the KDE can further improve the segmentation by relaxing the assumption of normality in the GMM. Once the foreground and background are found using GMM, the KDE can be applied to find their estimated densities. Then, a cut-off point for segmentation of pixels in a spot into two clusters is determinate by the cut-off point that has the near equality of two estimated densities. The details are reported below.

Algorithm for Segmenting One Spot by GKDE

Step 1: Segment a spot initially using the GMM algorithm in Section 2.3.2.

Step 2: Estimate the kernel densities for foreground (\hat{f}_f) and background (\hat{f}_g)

following the steps in Eqs. (5) – (7).

Step 3: Find a cut-off point (CP) that has the near equality of \hat{f}_f and \hat{f}_g .

Step 4: Segment a spot as follows.

$$x_i \in \begin{cases} \text{foreground, if } x_i \geq CP; \\ \text{background, elsewhere.} \end{cases}$$

2.3.4 Empirical Evaluation of the Performance for Segmentation Methods

Spike genes (or spots) with known contents on microarrays are used in the empirical studies. The target ratios of spike genes thus represent the gold standard for evaluating the accuracy of segmentation methods investigated in this study. The sum of squared relative error (SSRE) and the sum of squared error (SSE) are used to evaluate accuracy according to Eqs. (20) and (21):

$$SSRE = \sum_{j=1}^M \sum_{b=1}^B \left\{ \frac{\hat{T}_{j,b} - T_j}{T_j} \right\}^2, \quad (20)$$

$$SSE = \sum_{j=1}^M \sum_{b=1}^B (\hat{T}_{j,b} - T_j)^2, \quad (21)$$

where $\hat{T}_{j,b}$ is the feature estimated from the ratio of means between Cy3 and Cy5 arrays for the j^{th} spike gene in the b^{th} block, and T_j is target ratio of the j^{th} spike gene.

The number of blocks is $B = 32$ and the number of spike genes is $M = 8$. The smallness of SSRE and SSE indicate the closeness to target ratios. Table 2.3.4-1 and 2.3.4-2 present those two types of spike genes with various target contents and ratios used in this study.

Table 2.3.4-1: One set of eight spike genes with target contents and ratios in real microarrays.

Spike Gene	1	2	3	4	5	6	7	8
Target Content (Cy5: Cy3)	50:500	10:100	50:250	20:100	200:500	40:100	200:200	20:20
Target Ratio (Cy5: Cy3)	1:10	1:10	1:5	1:5	1:2.5	1:2.5	1:1	1:1

Table 2.3.4-2: Another set of eight spike genes with target contents and ratios in real microarrays.

Spike Gene	1	2	3	4	5	6	7	8
Target Content (Cy5: Cy3)	20:100	50:250	20:100	50:250	20:100	50:250	20:100	50:250
Target Ratio (Cy5: Cy3)	1:5	1:5	1:5	1:5	1:5	1:5	1:5	1:5

For those two types of spike genes, four sets of microarrays are produced and each set of microarrays consists of one pair of two dye-swapped microarrays. Therefore, each type of spike gene is associated with eight microarrays, of which a total of 16 microarrays are tested herein.

The Pearson and concordance correlation coefficient [46] of two random variables Y_1 and Y_2 is shown as Eq. (22) and (23):

$$\rho = \frac{Cov(Y_1, Y_2)}{\sqrt{\sigma_{Y_1} \sigma_{Y_2}}}, \quad (22)$$

$$\rho_c = \frac{2Cov(Y_1, Y_2)}{Var(Y_1) + Var(Y_2) + (E(Y_1) - E(Y_2))^2}. \quad (23)$$

These correlations are used in this study to measure the reproducibility among the expression of every gene and that of its duplicated spot using the log ratios of means in Cy5 to Cy3 dyes from one microarray image, which is expected to be close to 1.

These correlation coefficients of the swapped microarrays are also considered to evaluate the performance with reference to selected features with high log ratios of means in Cy5 to Cy3 dyes. As the dyes of Cy3 and Cy5 in the swapped arrays are exchanged, the negative correlation coefficient is obtained from the features of the swapped arrays and is expected to be close to -1.



3. Applications on MicroPET Images

This chapter explains the reconstruction and segmentation methods applied to microPET images. The FBP and OSEM are available methods of the built-in software of microPET manager V1.6.4 associated with the scanner to reconstruct microPET image. From our evaluation, the PDEM will demonstrate more accurate and less noisy reconstruction images than the FBP and OSEM. Moreover, the microPET manager V1.6.4 does not have any segmentation method for 3D images. Section 3.3 will present the GMM algorithm to segment 3D microPET images obtained from PDEM.

3.1 The MicroPET Scanner

The microPET R4 scanner in Taipei Veterans General Hospital is shown in Figure 3.1-1. The configuration of this microPET R4 has 32 rings, 6144 detectors, 7.3 cm field-of-view (FOV), and spatial resolution of 1.85 mm in the center. It can collect both prompt and delay sinograms. Transaxial projection bin size was 1.213 mm, and axial slice thickness was 1.2115 mm. Coincidence timing window was set at 6×10^{-9} seconds. The lower and upper level energy thresholds were 350 and 750 keV, respectively. Span of the data set was 3 (Appendix B.5), and maximum ring difference (MRD) of the data set was 31 (Appendix B.6). The target images were reconstructed using 128×128 pixels.





Fig. 3.1-1: The microPET R4 scanner in Taipei Veterans General Hospital is displayed.

A sinogram uses the polar coordinate system to store the response of a projection line (or a line of response, LOR) at a specific orientation with a radial distance from the FOV central axis as displayed in Figure 3.1-2.

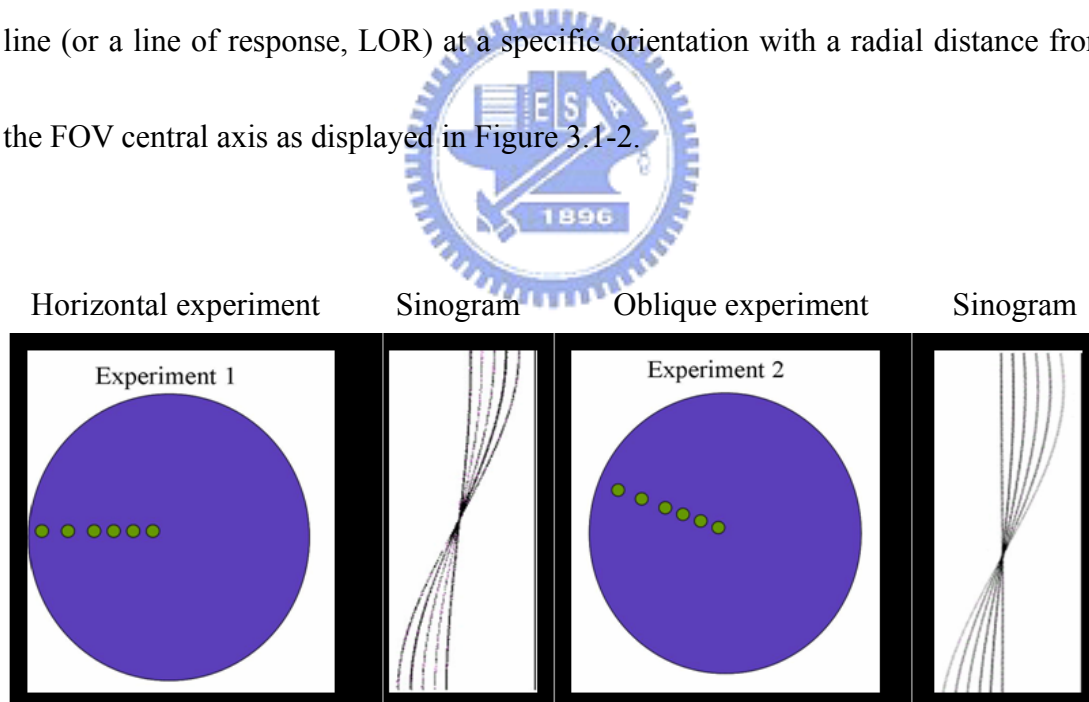


Fig. 3.1-2: Two images of microPET sinograms from physical experiments of six point sources are displayed. In every sonogram, the horizontal axis represents the ordering of line of responses (LORs) and the vertical axis represents different angles from 0 degree to 180 degree. The pixel intensity in the sinogram records total gamma rays detected in a scanning time window.

During scan acquisition, raw data are stored in sinograms, which are then used to reconstruct images. The prompt sinogram records coincidence events when two detectors receive two gamma rays within a specific time window (e.g., 6×10^{-9} second). The coincidence events in prompt sinograms include true, random, and scatter coincidence events. The delay sinogram records coincidence events when two detectors receive two gamma rays outside another specific time window (e.g., $3 \times 6 \times 10^{-9}$ second). The coincidence events in delay sinograms can be used to estimate random coincidence events.

The data matrices are described as follows (as in Fig. 3.1-3 and 3.1-4). First, list mode data were histogrammed into the 3D data with a span of 3 and MRD of 31, which are sized $2 \times 703 \times 96 \times 84$ (that is, 2 sinograms of prompt and delay windows $\times 703$ slices $\times 96$ angular views $\times 84$ projection lines (LORs) as in Fig. 3.1-3) and stored as floating type data. The second data were obtained using random pre-correction and were sized $1 \times 703 \times 96 \times 84$ (as in Fig. 3.1-4). These 3D data were rebinned into 2D sinograms using the FORE method with dead time and decay corrections. The attenuation, normalization, scattering, and arc corrections were not performed for simplicity as this study only focused on evaluation of random correction. These further corrections for PDEM reconstruction will need more investigation in future studies.

Two matrices were constructed using the software embedded in microPET R4 (that is, microPET manager V1.6.4). The first matrix was $2 \times 63 \times 96 \times 84$ (that is, 2 sinograms of prompt and delay windows \times 63 slices \times 96 angular views \times 84 projection lines (LORs) as in Fig. 3.1-3) and stored as floating type data. This matrix was reconstructed using the PDEM. The PDEM was compared with the built-in reconstruction schemes, such as 2D FBP and OSEM methods, in the microPET R4 system. The second matrix was obtained using the FORE and on-line random pre-corrected data (as in Fig. 3.1-4). The 2D OSEM, using 16 subsets with four iterations, and the 2D FBP, using ramp filtering, were applied to reconstruct the microPET images for comparison with the PDEM results. The reconstructed images were not smoothed.

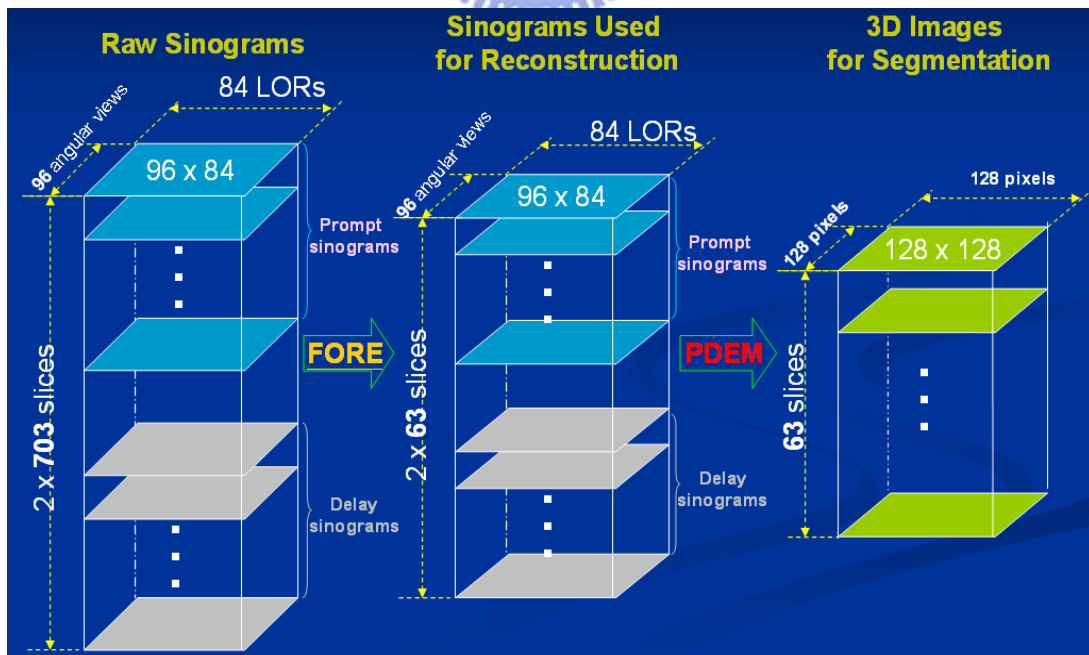


Fig. 3.1-3: The above data matrices are used for reconstruction by the PDEM and segmentation by the GMM.

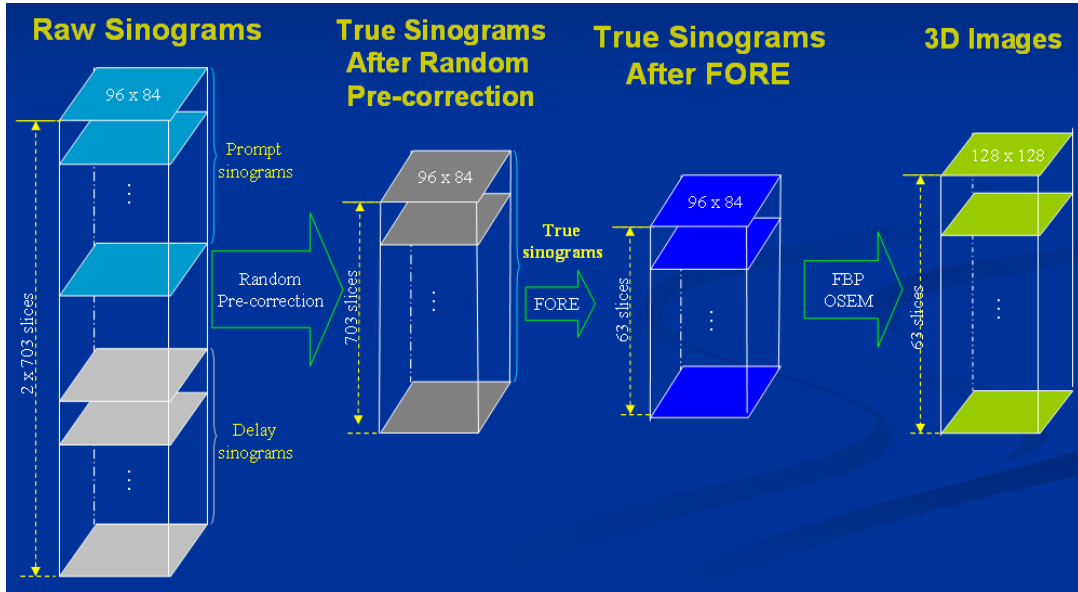
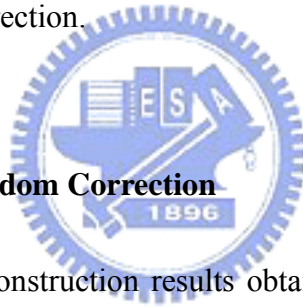


Fig. 3.1-4 The above data matrices are used for reconstruction by the FBP and OSEM with random pre-correction.



3.2 Reconstruction with Random Correction

This section shows the reconstruction results obtained from the PDEM, FBP and OSEM on simulation, phantoms, and real mouse microPET data.

3.2.1 Simulation Study

This study utilized the modified Shepp-Logan's head phantom as the simulated object to assess and compare the reconstruction images using the PDEM, FORE+FBP, and FORE+OSEM. We assumed that the simulated diameter of a ring was 28.28 mm and the FOV diameter was 20 mm. Target image was 128×128 pixels (20×20 mm²) and rescaled intensity was ≤ 100 . For each pixel intensity, $(\lambda_i(b))$ was simulated and then input into $\lambda_i^*(d)$. Then, $\lambda_i^*(d)$ is set to the multiplication of a given noise

ratio to $\lambda_i^*(d)$. At the end, n_p^* and n_d^* can be simulated using the Poisson distribution with parameters $\lambda_i^*(d)$ and $\lambda_i^*(d)$ as in Eqs. (1) and (2). Total counts (sum of prompt and delayed counts) were 276794, 316383 and 342407 with 5%, 10% and 30% noise levels, respectively, for the three slices simulated. The prompt and delayed sinograms had the same matrix size of 96×84 (that is, 96 angular views \times 84 projection lines (LORs)) with floating type data. Three random noise ratios of random to true coincidence counts, 5%, 10% and 30% were simulated. The quality of images obtained using the PDEM, FBP and OSEM were compared (Fig. 3.2.1-1). The simulated results demonstrate that the quality of images reconstructed by the PDEM is superior to that of images reconstructed by the FORE+FBP and FORE+OSEM.

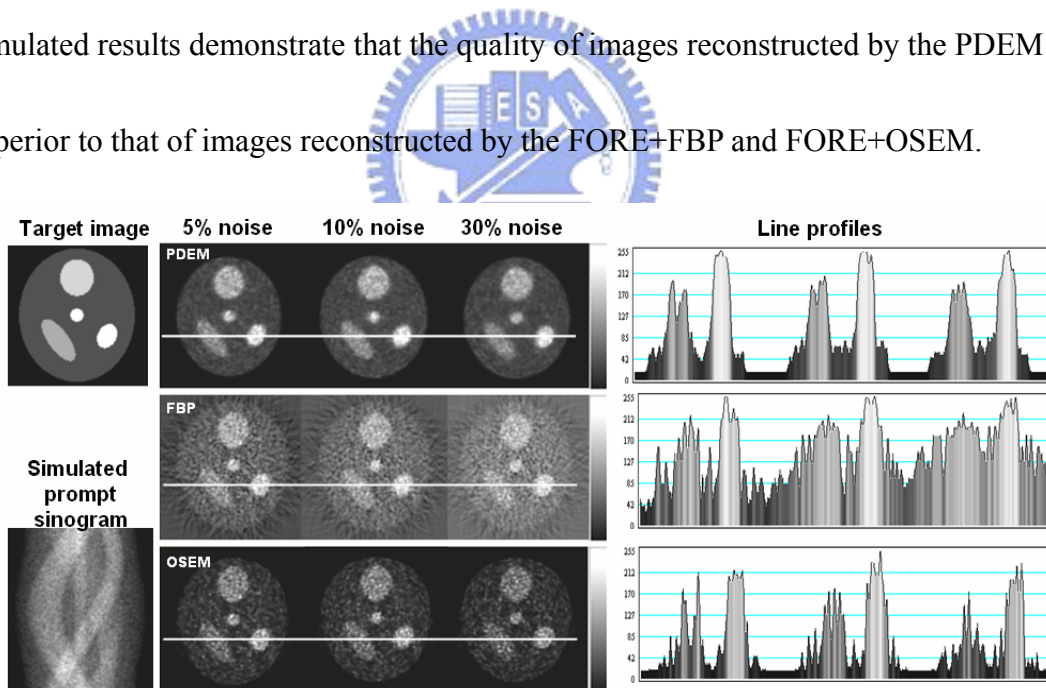


Fig. 3.2.1-1. The modified Shepp-Logan head image was used for simulation studies. The line profiles of PDEM were less noisy than those of FBP and OSEM. The PDEM technique reconstructed better images than the FBP and OSEM did with 5%, 10% and 30% random noise. All images were rescaled using their own maximum values.

3.2.2 Phantom Study

The first physical phantom was 28 homogenous line-sources with an outer diameter of 1.27 mm for each line. This phantom was utilized to assess the performance and accuracy of reconstruction quality between the FBP, OSEM and PDEM (as in Fig. 3.2.2-1). The spatial resolution was measured using the FWHMs from vertical and horizontal line profiles (in Table 3.2.2-1). The average and standard deviation of FWHMs in reconstruction images using the PDEM were smaller than those obtained by the FBP and OSEM.

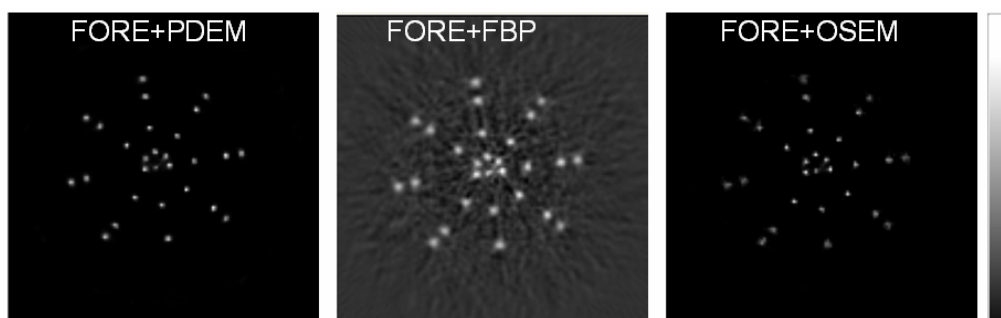


Fig. 3.2.2-1. The 31st slice of the 28 line-source phantom reconstructed using the three methods are displayed. Both FBP and OSEM are reconstruction methods built into the microPET R4 system. All images were rescaled using their own maximum values. The images are shown in the rectangular window. Table 3.2.2-1 presents the comparisons of their FWHMs.

Table 3.2.2-1: Average and standard deviation (in mm) of 28 FWHMs for horizontal and vertical line profiles measured for comparing the spatial resolutions of PDEM, OSEM and FBP. Those values are measured at the 31st slice.

Methods	Horizontal profile		Vertical profile	
	Average	Standard deviation	Average	Standard deviation
PDEM	1.779	0.324	1.790	0.311
OSEM	1.890	0.527	1.863	0.548
FBP	3.641	0.595	3.663	0.624

The second phantom was a uniform cylinder of 7.6 cm high with an inner radius of 20 mm. This phantom was also utilized to compare image quality obtained using the FBP, OSEM and PDEM. Imaging scan time was 1200 s using the microPET R4 after injection of 276 μCi F-18 FDG. Three reconstruction techniques were applied to reconstruct the 40th slice (in Fig. 3.2.2-2). Reconstruction images were presented with the associated central line profiles. Reconstruction images obtaining using the PDEM had better quality than those generated by the FBP and OSEM on their line profiles. A circular region of interest (ROI) was employed to measure the noise level for the different reconstruction methods. The lowest value for coefficient of variation (CV), which is the ratio of standard deviation to mean, was obtained by using the PDEM reconstruction (in Table 3.2.2-2).

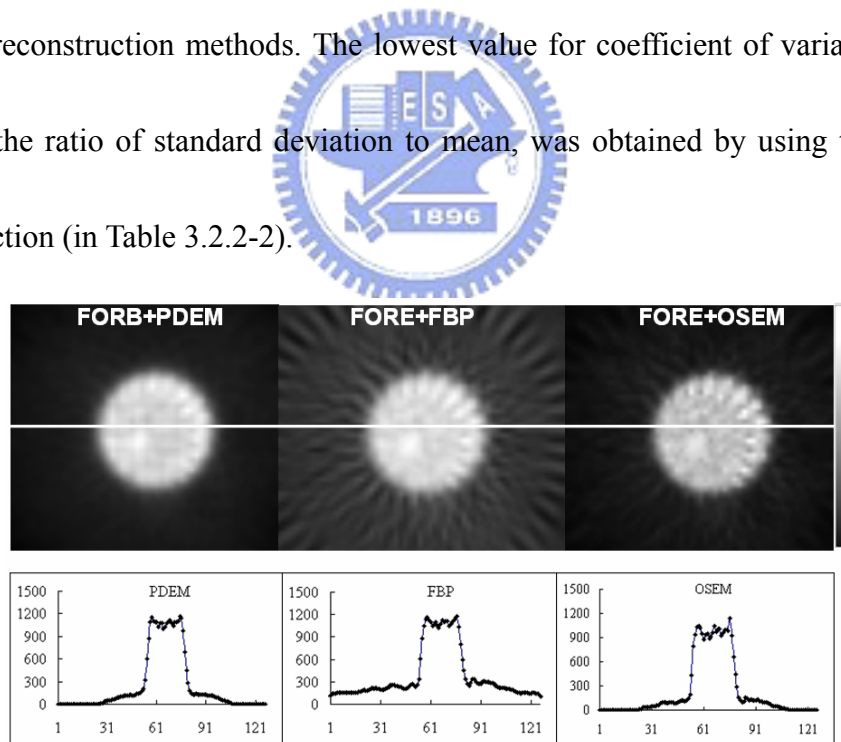


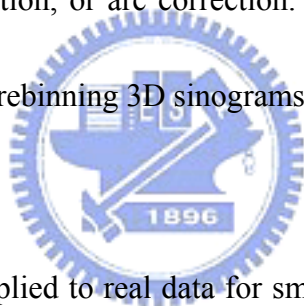
Fig. 3.2.2-2. The reconstructed 40th slice from a uniform phantom was used to investigate noise level generated by the three approaches. The white line indicates the position of the investigated line profile. All images were rescaled using their own maximum values. The images are shown in the rectangular window with enlarged central parts. Table 3.2.2-2 presents the comparisons of their CVs.

Table 3.2.2-2: A circular ROI with a radius of 9 pixels to the center of the uniform phantom was utilized to compare noise levels between the PDEM, FBP and OSEM. Those values were measured at the 40th reconstructed slice.

	PDEM	FBP	OSEM
Average	1146.51	1107.66	1105.36
Standard deviation	36.26	46.82	65.56
Coefficient of variation (%)	3.16	4.23	5.93

The PDEM reconstructed better quality images with lower noise levels than the reconstructed approaches built into the microPET R4 system during investigations of line and uniform phantoms. Notably, in all reconstruction processing, there was no attenuation, scatter, normalization, or arc correction. However, dead time and decay correction were applied when rebinning 3D sinograms into 2D data.

3.2.3 Real Mouse Study



The PDEM method was applied to real data for small mice to compare the quality of reconstructed images with those reconstructed using the FBP and OSEM. These two real normal mice weighed 20 g. Imaging scan time was 600 second using the microPET R4 following an injection of 0.226 μ Ci F-18 FDG for the first mouse and an injection of 240.5 μ Ci F-18 FDG for the second mouse. The first mouse was utilized to investigate reconstruction performance under a weak amount of F-18 FDG activity. The second mouse was used to investigate image quality under a normal amount of F-18 FDG.

All 63 slices after the FORE were reconstructed using the PDEM, FBP and OSEM.

Figures 3.2.3-1 and 3.2.3-2 present coronal and sagittal images of the two mice reconstructed by the PDEM. These images are less noisy and have clearer boundaries than those reconstructed by the FBP and OSEM. These results demonstrate that the PDEM reconstructed images with better contrast and clearer boundaries than those reconstructed with the FBP and OSEM.

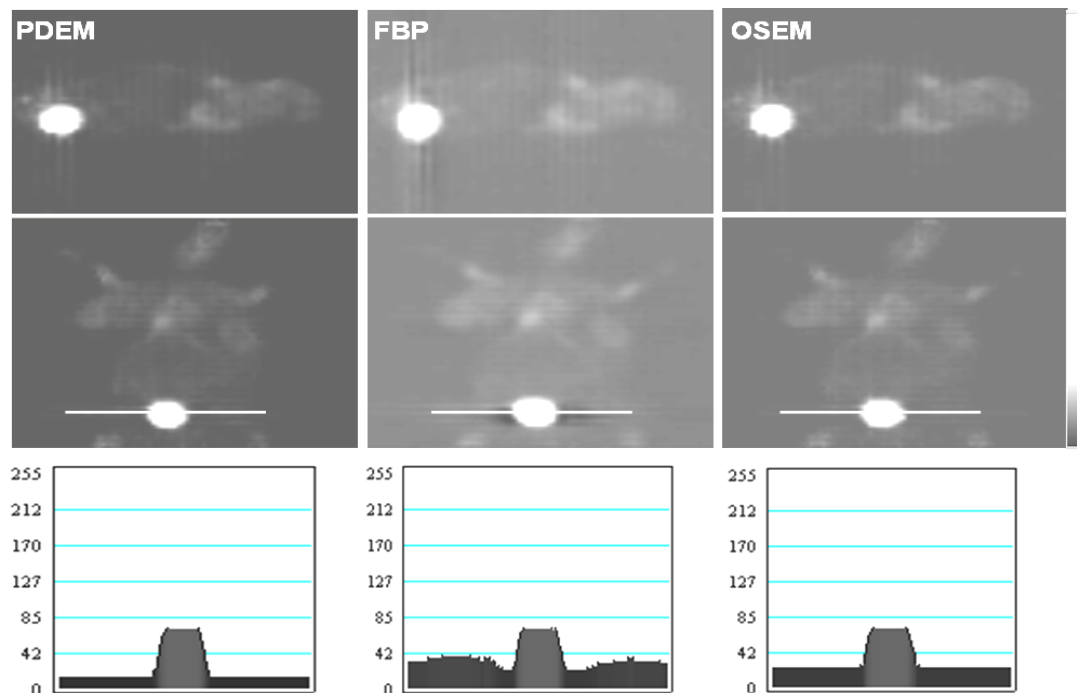


Fig. 3.2.3-1: Sagittal (top) and coronal (middle) images of the first mouse image reconstructed by PDEM (left), FBP (middle) and OSEM (right). The images reconstructed by PDEM have less noise than those reconstructed using FBP and OSEM with comparison by line profiles. The images are shown in the rectangular window with enlarged central parts.

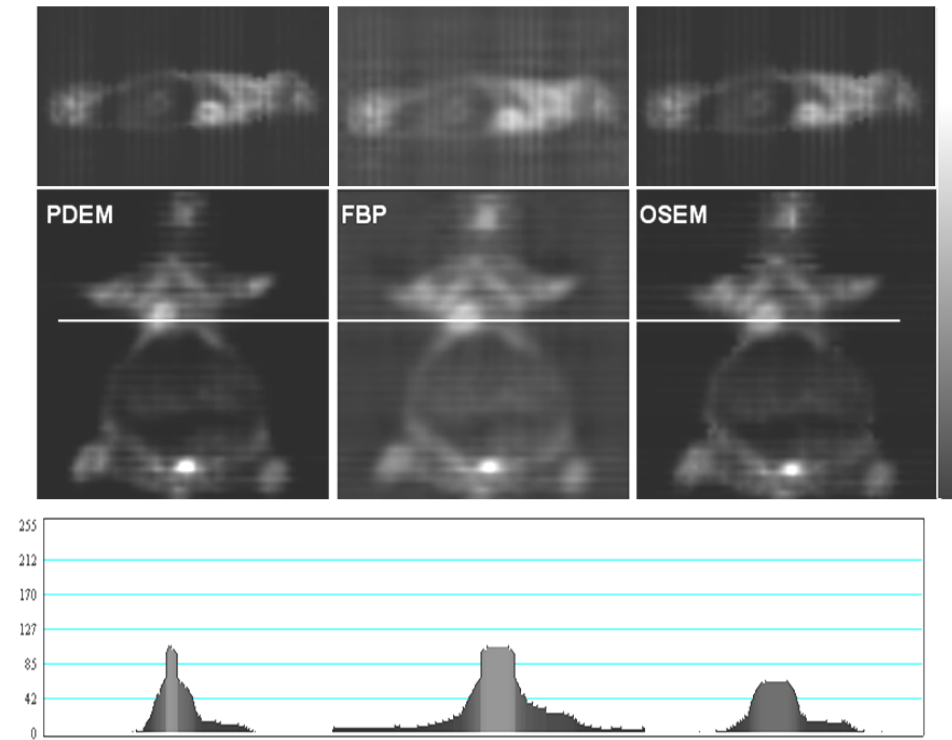


Fig. 3.2.3-2. Coronal and sagittal images of the second mouse image reconstructed using PDEM (left), FBP (middle) and OSEM (right). The images reconstructed by PDEM have less noise than those reconstructed by FBP and OSEM, as shown in the respective line profile near the heart. The images are shown in the rectangular window with enlarged central parts.

3.3 Segmentation of 3D MicroPET Images

This section introduces the use of GMM to segment 3D microPET images from the reconstruction images by the PDEM.

3.3.1 3D Images

Figure 3.1-3 shows the data matrices used for reconstruction and segmentation. There are 703 sinograms obtained by the 3D microPET with span 3 and MRD 31. We applied the FORE on prompt and delay sinograms to obtain 63 sinograms. Each 2D sinogram was reconstructed by the PDEM. In this study, each slice has the size of 96

x 84 and each reconstructed images has the size of 128 x 128. A matrix with the dimension of 63 x 128 x 128 was used for segmentation by the GMM and K-means algorithms. The analysis flow chart to segment 3D images is displayed in Fig. 3.3.1-1.

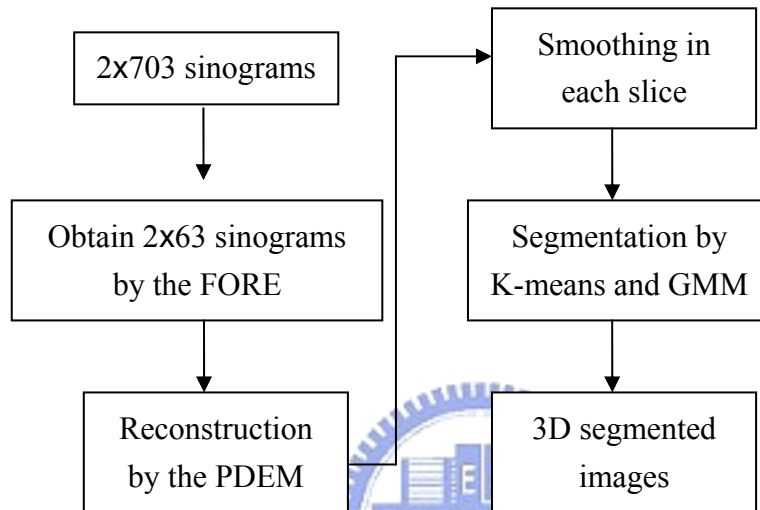


Fig. 3.3.1-1. The flow chart of 3D segmentation is plotted.

The PDEM is the reconstruction process of microPET images. The GMM or K-means are applied algorithms for segmentation. The phantoms for simulation studies are displayed as Fig. 3.3.1-2. There are 63 reconstructed slices with the size of 128 x 128.

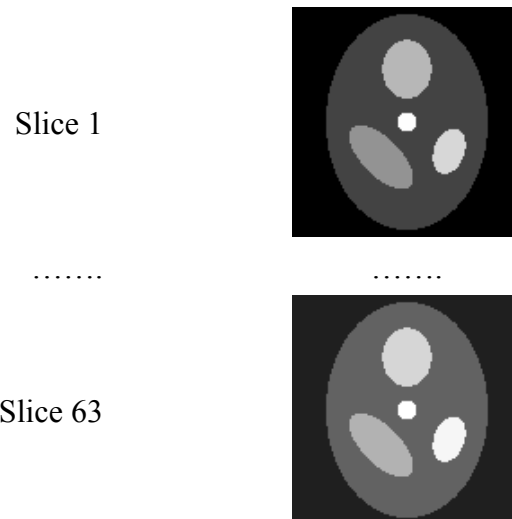


Figure 3.3.1-2: 3D microPET images for 63 slices are illustrated. Every image has the pixels size of 128 by 128.

3.3.2 Simulation Study

The simulated phantom study with 457932 total counts is displayed in Figure 3.3.2-1. This simulated study is focused on testing and evaluating the performance of GMM. Figure 3.3.2-1A shows target image with five ROIs. Figure 3.3.2-1B displays target image with 50% noise added. Figure 3.3.2-1C presents the clustering results by GMM. The number of clusters is decided by the KDE and is shown in Figure 3.3.2-1D. There are four local high peaks that are regarded as the means of four clusters.

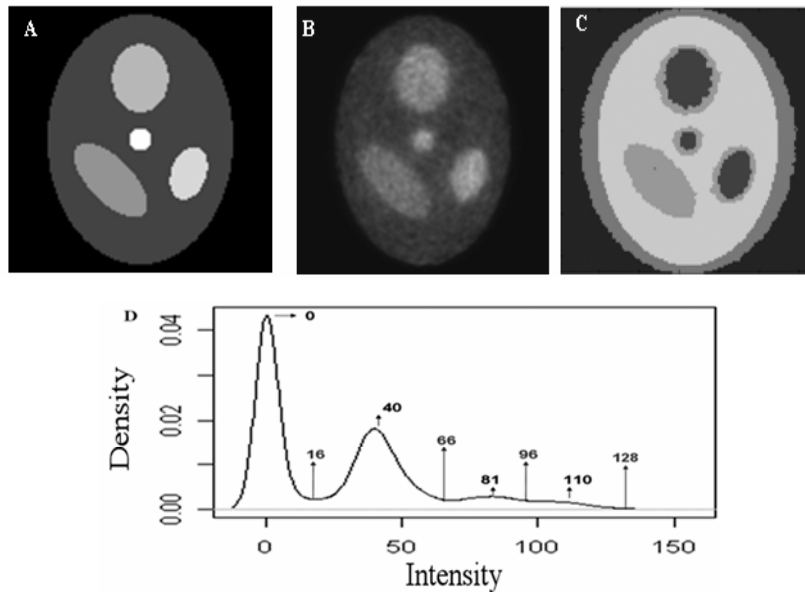


Fig. 3.3.2-1. **A)** Simulation image of five clusters is displayed. **B)** Adding 50% noise into panel A. **C)** Clustering results using GMM. **D)** Kernel density curve using **C)** with values of high and low peaks. Four peaks are identified on the density curve. Hence, the number of groups is set as four.

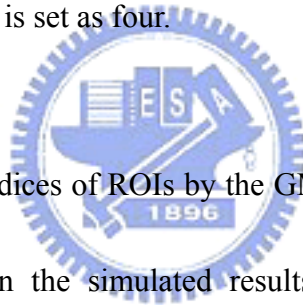


Figure 3.3.2-1 shows the indices of ROIs by the GMM. Figure 3.3.2-3 presents the accuracy comparison between the simulated results obtained from K-means and GMM.



Fig. 3.3.2-2. Target ROIs are marked.

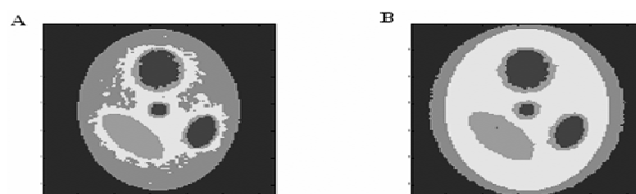


Fig. 3.3.2-3. The results of **A)** by K-means and **B)** by GMM clustering are shown.

It is observed that the GMM has a clearer segmentation result than the K-means method. Results of ROIs are shown in details in Table 3.3.2-1. The total accuracy of GMM is 92.1% and that of K-means is 66.6%.

Table 3.3.2-1: Comparisons of the clustering results by K-means and GMM in Fig. 3.3.2-1A.

ROI #	True Pixel Count	Exact Counts		Accuracy (%)	
		K-means	GMM	K-means	GMM
ROI 1	6604	4128	6206	62.5%	94.0%
ROI 2	702	488	522	69.5%	74.4%
ROI 3	748	700	745	93.6%	99.6%
ROI 4	350	280	285	80.0%	81.4%
ROI 5	88	58	59	65.9%	67.0%
Total	8492	5654	7817	66.6%	92.1%

Another simulated volume data based on the modified Shepp-Logan's head phantom image is shown in Figure 3.3.2-4A and 3.3.2-4B. Fifty percentage of noise ratio to phantom images are added. In order to compare the effects of variation between slices, different image levels and shapes of ROIs are considered in slice 1 and 2. First, we use the MLEM reconstruction, the result is shown in Figure 3.3.2-4C and 3.3.2-4D. Meanwhile, the GMM is also applied to segment two images without slice normalization as shown in Figure 3.3.2-4E and 3.3.2-4F. It is observed that the boundaries of ROIs are difficult to distinguish. Therefore, slice normalization is applied to the volume data and then the GMM is used to segment images as shown in Figure 3.3.2-4G and 3.3.2-4H. The boundaries of these segmentations become clearer after slice normalization. Figure 3.3.2-4I plots the estimated kernel density curve of volume data for finding the number of clusters and initialized values.

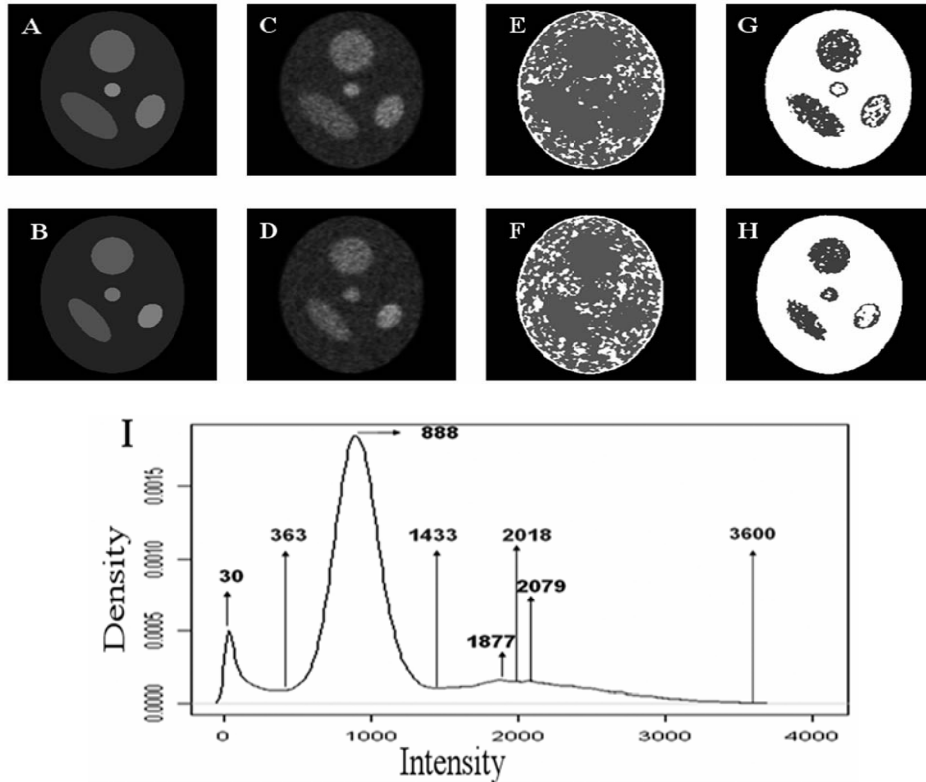


Fig. 3.3.2-4. Simulated volume data including slice 1 and 2 are marked as **A** and **B**. **C** and **D** are reconstructed images after added 50% noise ratio to **A** and **B**. **E** and **F** are segmented results without slice normalization. **G** and **H** are segmented results with slice normalization. **I** is the estimated kernel density curve of simulated volume data after slice normalization.

For these simulation cases, the performance and accuracy using GMM is better than those of using K-means. The KDE is adopted to decide the number of clusters and the starting values of parameters in the EM algorithm. The slice normalization is necessary when the GMM is applied to segment volume data in this study.

3.3.3 Real Mouse Study

The empirical data of a big mouse injected by F-18 isotope scanning is collected from the microPET R4 system. The acquired configurations are listed as below.

Scanner energy is between 350 and 750 keV with the total scanning of 3600 s. There are 32 rings in microPET R4 system. File format of histogram data is stored by 2 bytes for each voxel. Ten slices (from the 51st to the 60th slice) of the volume data are used for investigation and evaluation.

Figure 3.3.3-1 shows the estimated kernel density curve of volume data. Based on this KDE, four groups are determined by local high peaks and their starting values are obtained for applying the EM algorithm.

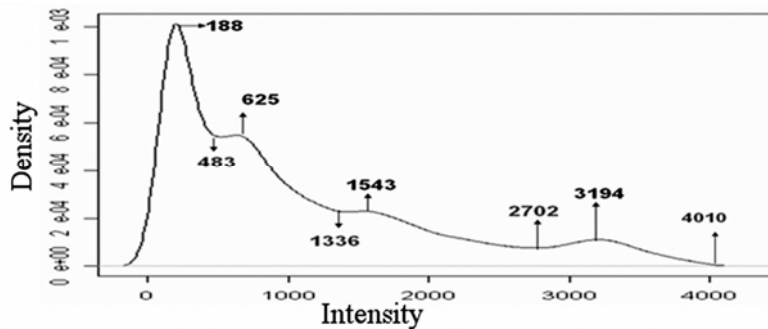


Fig.3.3.3-1. The estimated kernel density curve using the rat volume data of 10 slices is shown with values of high and low peaks. There are four peaks. Hence, the number of groups is set as four. Values of peaks are applied to compute the starting values in EM algorithm.

Figure 3.3.3-2 shows the reconstructed rat images by MLEM from the 51st to the 60th slice. Besides, Figure 3.3.3-3 and 3.3.3-4 show the segmentation results by GMM and K-means respectively. The detail segmentation from GMM is shown with the comparison to Figure 3.3.3-5. The uptake areas can be segmented by GMM from 59th and 60th images. In addition, it can segment small areas with high gene expression when compared to K-means. On the contrary, the K-means method segments big areas and ignores small uptake areas.

For this real mouse study by microPET, the GMM leads to more detail segmentation results than the K-means method does. The GMM also has better performance than K-means. The full width half maximum (FWHM) is usually used to evaluate performance of segmented results. The horizontal line profile near the center of the 60th slice is used to investigate the performance between GMM and K-means. Figure 3.3.3-5 is plotted with four regions in this line profile and their FWHMs for Fig. 3.3.3-2.

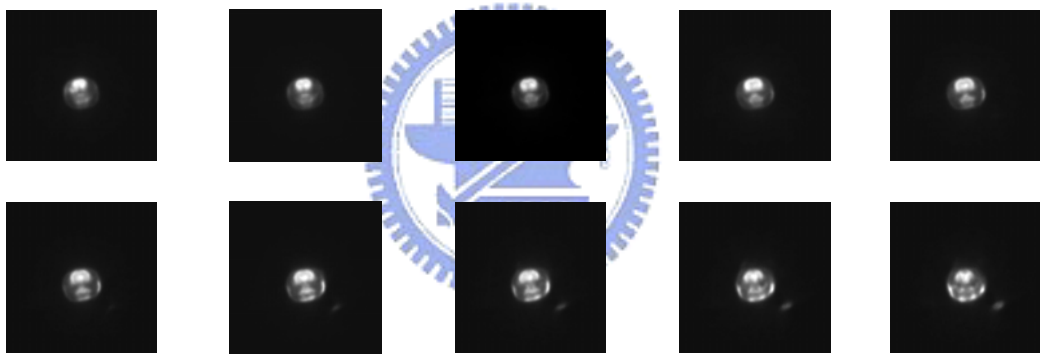


Fig. 3.3.3-2. The reconstructed rat images are shown from the 51st (top-left) to the 60th (bottom -right) slice.

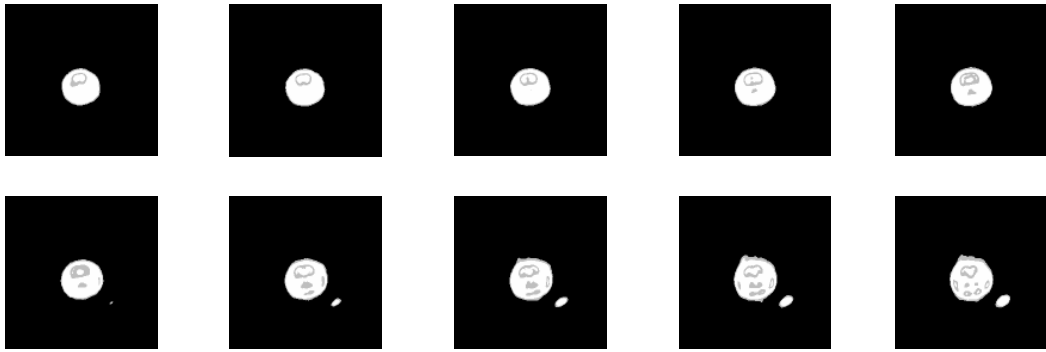


Fig. 3.3.3-3. The results of segmentation by the GMM are shown from the 51st (top-left) to the 60th (bottom -right) slice.

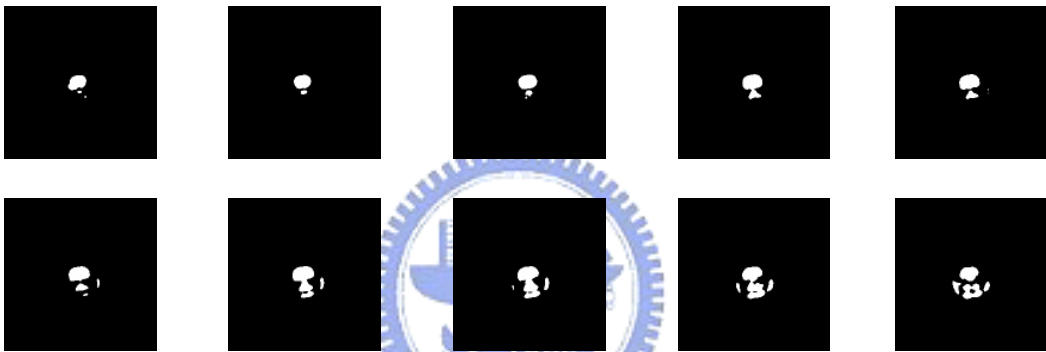


Fig. 3.3.3-4. The results of segmentation by the K-means are shown from the 51st (top-left) to the 60th (bottom -right) slice.

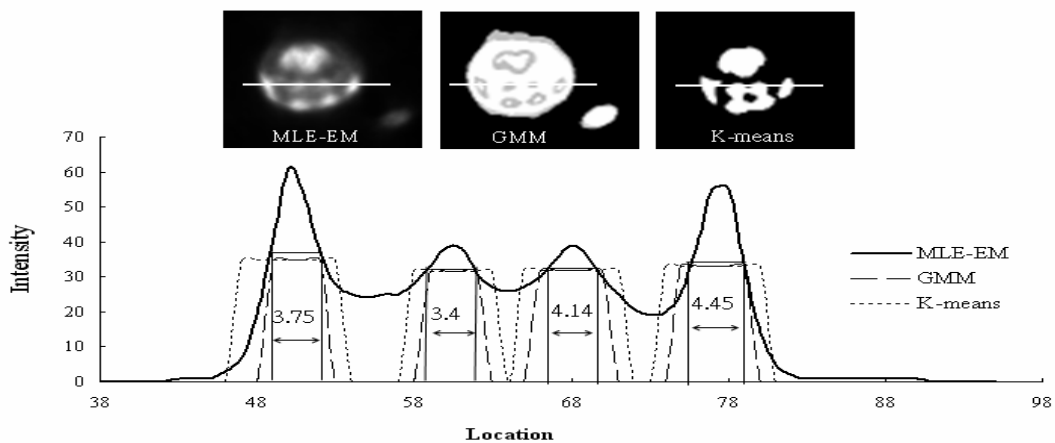


Fig. 3.3.3-5. The horizontal line profile of the 60th slice of Fig. 3.3.3-2 is shown with FWHMs. The FWHMs of region 1, 2, 3 and 4 are 3.75, 3.40, 4.14 and 4.45 pixels respectively. The top part shows the location of this line profile in the MLEM reconstruction image and the segmentation by GMM and K-means.

Table 3.3.3-1 shows that the FWHMs of segmented results by GMM are closer to target FWHMs than those by K-means. Meanwhile, the signal to noise ratio (SNR) defined by the ratio of mean value to standard deviation is used to compare the segmentation performance between GMM and K-means. The SNRs of four regions of GMM are higher than those of K-means.

Table 3.3.3-1: The FWHMs and SNRs of segmented results by GMM are better than those by K-means in Fig. 3.3.3-5.

Region	FWHM of Region	Pixel of Boundary		Signal to Noise Ratio (SNR)	
		GMM	K-means	GMM	K-means
1	3.75	4	7	9.83	6.82
2	3.40	4	6	8.64	6.23
3	4.14	5	7	4.05	2.13
4	4.45	5	7	3.15	2.13

4. Applications on Microarray Images

This chapter investigates the applications of segmentation methods on spotted microarray images. The GMM and KDE are both employed to segment spotted images. Furthermore, we combine GMM and KDE to form a new method, GKDE, to segment spots. The GKDE can keep advantages of KDE and refining the final results from the GMM. We will compare and evaluate the performance of three methods together with the adaptive irregular segmentation method in GenePix 6 based on spike genes, duplicated genes, and swapped arrays in real microarray data.

4.1 The Spotted Microarray Image

These 16 real microarray images used herein are obtained by swapping Cy3 and Cy5 dyes. Each array has 32 blocks, 15488 spots with 7744 genes. Two replicated spots are designed in one array, of which the upper 16 blocks are duplicated as the lower 16 blocks in Fig. 4.1-1. Meanwhile, eight spike genes are designed in each block to evaluate the performance and accuracy of segmentation methods as shown in Fig. 4.1-1.



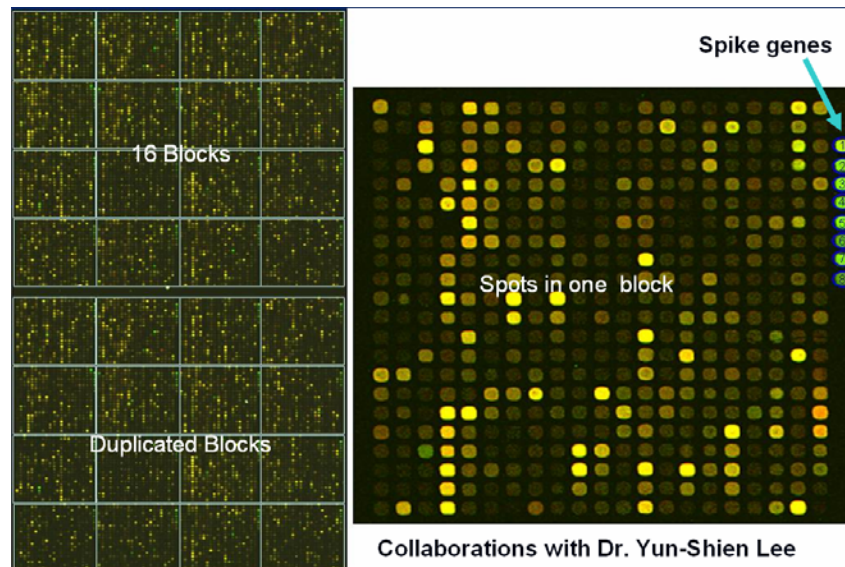


Fig. 4.1-1: An example of microarray image with 32 blocks, 22 columns and 22 rows. One block is enlarged and eight spike genes are numbered.

A typical spot diameter on each microarray in this study is approximately 160 μm . Sixteen microarray experiments were conducted in Genomic Medicine Research Core Laboratory of Chang Gung Memorial Hospital, Taiwan. The details of the microarray experiment procedure and probe information are available on the webpage of the laboratory,

http://www.cgmh.org.tw/intr/intr2/c32a0/chinese/corelab_intro/genetics/files/03OctClone_information_F.zip,

[http://www.cgmh.org.tw/intr/intr2/c32a0/chinese/corelab_intro/genetics/files/MIAME%20\(GMRCL%20Human%207K\)_ver01.zip](http://www.cgmh.org.tw/intr/intr2/c32a0/chinese/corelab_intro/genetics/files/MIAME%20(GMRCL%20Human%207K)_ver01.zip), and in [42]. These eight pairs of swapped microarrays were used for cancer research. Some of the results have been published [43]. Figure 4.1-2 presents one of the results by the adaptive irregular

segmentation in GenePix 6.0 for spot images of Cy3 and Cy5 dyes. The segmentation region may be inaccurate, leading to an over- or under- estimation of the statistics on spot intensities.

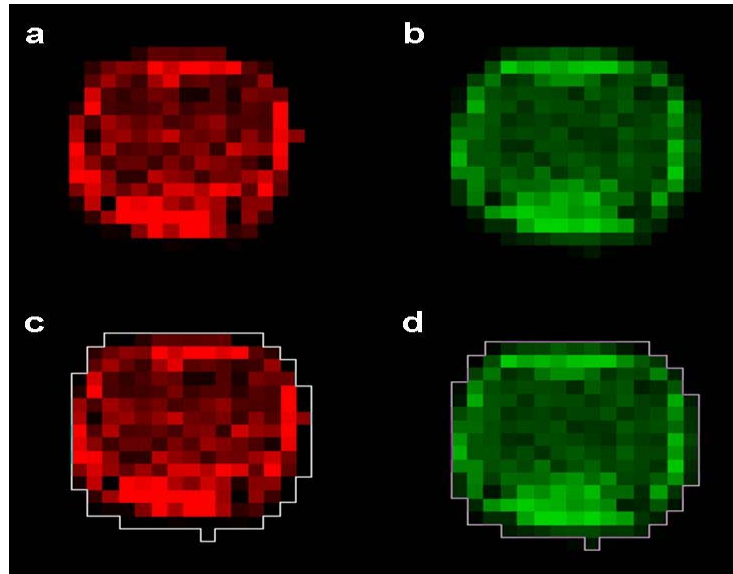


Fig. 4.1-2: Typical segmentation of two spot images by the irregular segmentation method of GenePix 6.0. Parts a) and b) present the original images of Cy5 and Cy3 dyes. Parts c) and d) present the segmented region on the images of Cy5 and Cy3 dyes.

Figure 4.1-3 plots the estimated kernel density curves from spot images of Cy3 and Cy5 dyes using the R 2.4.0 software [41, <http://finzi.psych.upenn.edu/R/library/stats/html/density.html> and <http://www.r-project.org/>]. These estimated densities typically have two distributions in the foreground and background regions.

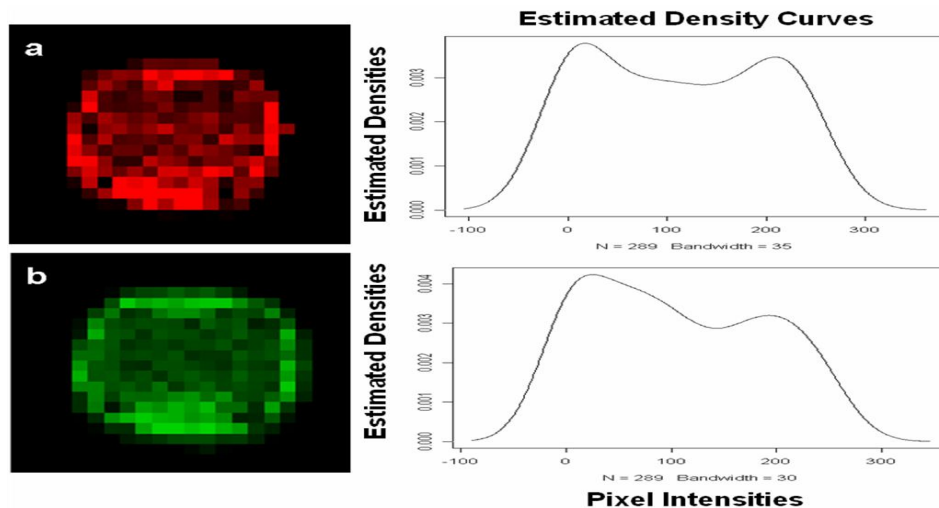


Fig. 4.1-3: Two estimated density curves for spot of Cy5 (a) and Cy3 (b) dyes. Both Cy3 and Cy5 images have two intensity distributions for background and foreground pixels. The local minimum is used to be cutting point for segmenting spot pixels.

4.2 Evaluation from Spike Genes

There are 256 spike genes on any array with different known Cy3 and Cy5 ratios. Those spike genes are used to detect performance of GKDE, KDE, GMM and GenePix 6. Fig. 4.1-1 presents the locations and numbers of spike spots in one example of cDNA microarray images. Table 4.2-1 and 4.2-2 shows that all of the SSREs and the SSEs obtained from KDE are smaller than those obtained by the irregular segmentation method in GenePix 6.0, according to a test based on 16 real microarray cDNA images.

The relative improvements of these two segmentation methods are defined as the percentages of the evaluation values in $(GenePix-Methods)/GenePix$. Since the first eight arrays are produced according to Table 2.3.4-1 that have varying target ratios,

the relative improvements measured by SSRE and SSE are different according to Eqs. (20) and (21). The last eight arrays are produced according to Table 2.3.4-2 that has a constant ratio, the relative improvements measured by SSRE and SSE are the same according to Eqs. (20) and (21). Table 4.2-1 and 4.2-2 shows that the average relative improvements of GKDE, KDE and GMM associated with the irregular segmentation method in GenePix 6.0 for SSRE and SSE are at the level of (23.5%, 20.9%), (10.5%, 9.2%), and (23.2%, 20.9%). These results reveal that the features estimated by GKDE, KDE and GMM are closer to the designed target ratios for the spike genes than those obtained by the irregular segmentation method in GenePix 6.0.

Table 4.2-1: The comparisons of SSEs are obtained for different methods based on spike genes. Array 1s is that obtained by swapping the dyes of Array 1. Relative improvement is specified by $(GenePix-Method)/GenePix$ as a percentage.

Array	Sum of Square of Errors				Relative improvement		
	GKDE	KDE	GMM	GenePix	GKDE	KDE	GMM
1	160.4	180.2	160.6	185.6	13.57	2.87	13.44
1s	116.3	134.2	117.1	146.3	20.49	8.21	19.96
2	136.7	145.6	136.9	153.1	10.71	4.90	10.56
2s	729.0	878.6	729.9	904.5	19.40	2.86	19.30
3	134.4	148.6	135.3	158.5	15.21	6.23	14.60
3s	405.8	534.9	406.1	691.0	41.28	22.58	41.23
4	51.7	68.3	52.2	83.4	37.98	18.10	37.42
4s	300.0	308.9	300.3	318.1	5.69	2.91	5.62
5	231.6	258.8	232.5	276.2	16.14	6.29	15.82
5s	237.3	299.6	237.6	349.7	32.15	14.32	32.06
6	140.7	166.2	141.4	172.2	18.32	3.49	17.89
6s	146.5	173.3	147.4	185.9	21.18	6.81	20.71
7	127.5	157.2	128.4	175.9	27.51	10.65	27.01
7s	67.3	79.0	68.3	122.4	44.98	35.41	44.22
8	133.5	148.6	133.8	177.9	24.94	16.46	24.79
8s	107.4	137.7	108.3	145.9	26.42	5.63	25.78
Average Relative Performance					23.50	10.48	23.15

Table 4.2-2: The comparisons of SSREs are obtained for different methods based on spike genes.. Array 1s is that obtained by swapping the dyes of Array 1. Relative improvement is specified by $(GenePix-Method)/GenePix$ as the percentage.

Array	Sum of Square of Relative Errors				Relative improvement		
	GKDE	KDE	GMM	GenePix	GKDE	KDE	GMM
1	8755.8	9624.5	8756.1	9739.2	10.10	1.18	10.09
1s	6146.4	7106.5	6147.2	7662.9	19.79	7.26	19.78
2	6768.2	7227.2	6768.4	7604.2	10.99	4.96	10.99
2s	25079.2	26518.8	25080.1	27604.5	9.15	3.93	9.14
3	6873.6	7595.9	6874.5	7968.9	13.75	4.68	13.73
3s	9923.7	11503.9	9924.0	12979.6	23.54	11.37	23.54
4	2640.0	3645.9	2640.4	4230.4	37.60	13.82	37.58
4s	16359.1	16560.6	16359.3	16621.4	1.58	0.37	1.58
5	5811.8	6470.4	5812.6	6905.1	15.83	6.29	15.82
5s	5939.3	7490.2	5939.6	8742.5	32.06	14.32	32.06
6	3527.9	4155.3	3535.3	4305.7	18.07	3.49	17.89
6s	3684.6	4331.5	3685.4	4648.1	20.73	6.81	20.71
7	3208.8	3929.1	3209.7	4397.2	27.03	10.65	27.01
7s	1705.5	1975.9	1706.4	3059.2	44.25	35.41	44.22
8	3344.0	3714.8	3344.2	4446.6	24.80	16.46	24.79
8s	2707.0	3443.1	2708.0	3648.6	25.81	5.63	25.78
Average Relative Performance					20.94	9.16	20.92

4.3 Evaluation from Duplicated Genes and Swapped Arrays

Table 4.3-1 shows the numbers of used spots excluding spike spots and bad spots in each array and its swapped array.

Table 4.3-1: Used spots excluding spike spots and bad spots in each array are listed and “x2” means two duplicates on every array.

Array	Used Spots	Call Rate %
1, 1s	7281x2	94.02%
2, 2s	7306x2	94.34%
3, 3s	7253x2	93.66%
4, 4s	7292x2	94.16%
5, 5s	7292x2	94.16%
6, 6s	7347x2	94.87%
7, 7s	7085x2	91.49%
8, 8s	7280x2	94.01%

The bad spots are defined by negative values of foreground minus background mean provided from GenePix 6.0. Those genes are used to investigate performance of GKDE, KDE, and GMM. Figure 4.3-1 shows agreement scatter plots of two replicates gene expression and swapped arrays using GKDE, KDE, GMM and Genepix 6 respectively. The KDE has less outliers than the GKDE, GMM and GenePix 6. In addition, the GKDE and GMM have less outliers than the GgenePix 6.

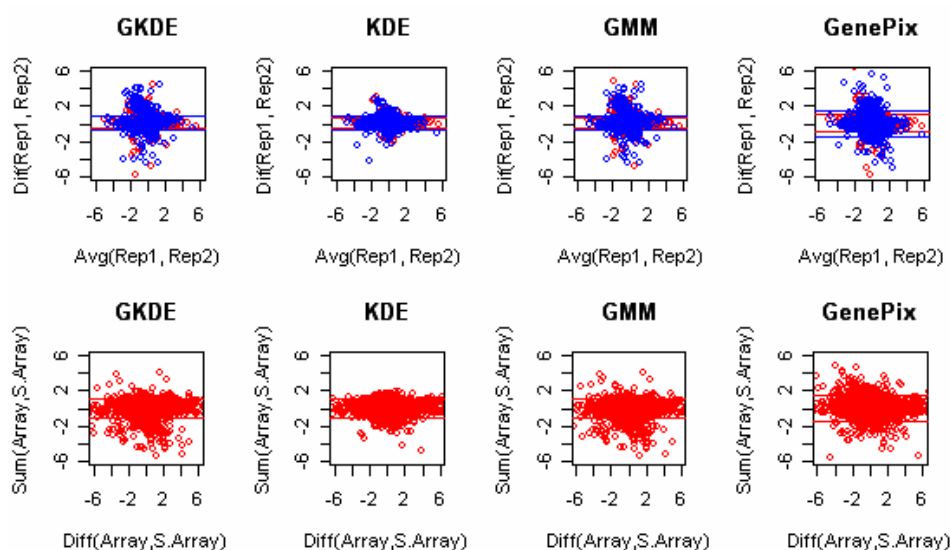
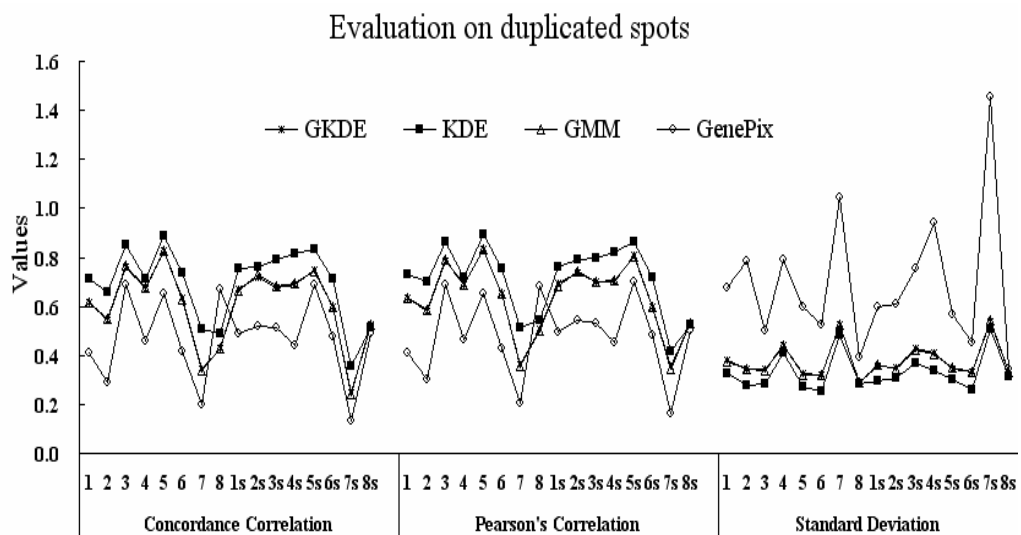


Fig. 4.3-1: Top row shows four methods to evaluate duplicated spots for 3rd (red) and swapped 3rd (blue) arrays. The x-axis and y-axis represent average and difference between duplicated spots. Bottom row shows four methods to evaluate swapped arrays (3rd, 3rd s). The x-axis and y-axis represent summation and difference between swapped arrays.

Figure 4.3-2 shows the concordance correlation coefficients, Pearson's correlations and standard deviations between replicates gene expression of sixteen arrays and eight swapped arrays.



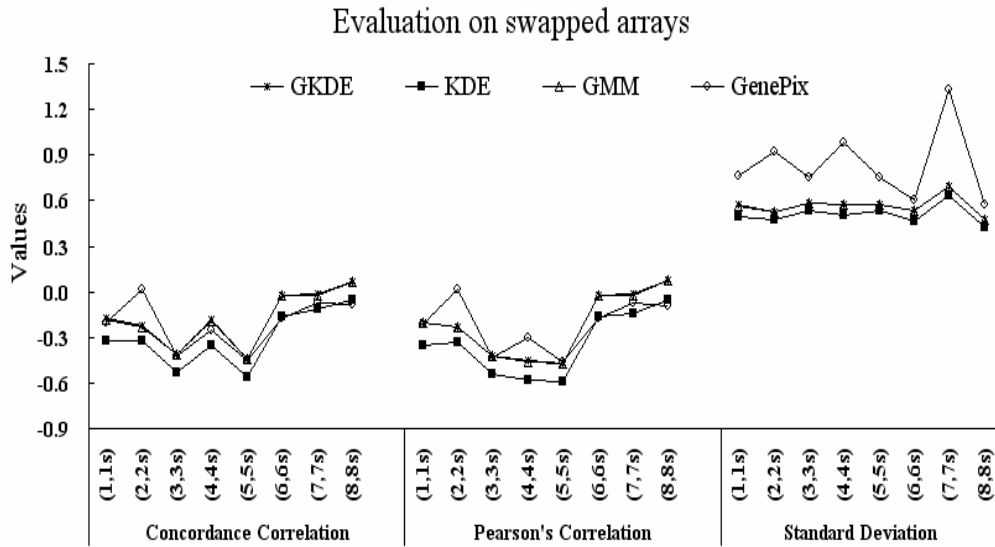
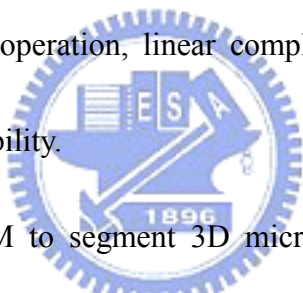


Fig. 4.3-2: Top and down figure are concordance correlations, Pearson's correlations and standard deviations between duplicated spots of sixteen arrays and between swapped arrays of eight arrays using the GKDE, KDE, GMM and GenePix 6.

The KDE has produced higher correlation and lower standard deviation than those by other methods tested on sixteen arrays with duplicated genes. And the same results as tested on swapped arrays, the KDE has provided lower standard deviation and higher correlation between tested eight swapped arrays. In addition, the GKDE and GMM both have higher correlations and lower standard deviations that the GenePix 6.

5. Discussion and Conclusion

The proposed PDEM algorithm for microPET reconstruction with random correction is demonstrated to produce less noise level, high spatial resolution, and clear boundary of image than those of FORE+OSEM and FORE+FBP from the comparison studies of simulation, phantoms, and real mouse microPET data. Meanwhile, the PDEM method reconstructs images with lower CVs and smaller FWHMs than those generated by methods built into the microPET R4. In addition, the PDEM method has the same advantages as the MLEM method in PET reconstruction—namely, row operation, linear complexity, monotonic convergence, non-negativity and parallelizability.



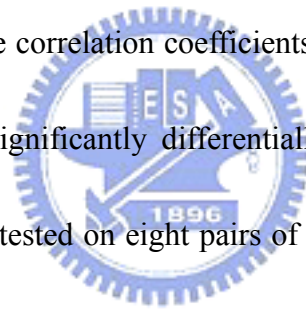
We have applied the GMM to segment 3D microPET images after the PDEM reconstruction. The GMM can model the segments of 3D microPET images with different distribution parameters. On the other hand, the K-means method proposed in literatures for segmentation microPET images assumed a constant variance for all clusters. Hence, the GMM approach is more flexible and accurate to model and segment microPET 3D images than K-means. The GMM proposed in this study can also perform the segmentation automatically through the initial estimated from the KDE method. On the other side, the seeding region growing methods proposed in literature for the segmentation of PET images, initial seeds were crucial to perform

images segmentation. The number of clusters was determined by a subjective choice or sequentially searching including the K-means method. When the activities of various clusters have different patterns, the slice normalization approach incorporated with GMM is useful to segment 3D images. For further investigation, it will be of great interest to further evaluate the qualitative and quantitative performance by more phantom and empirical studies with the comparisons to judgments from medical experts.

The GMM and KDE methods are also applied to spotted microarray images. The effect of expression profiling on prognostic and predictive testing for cancer has been recently discussed [47]. However, the low reproducibility of microarray experiments [48, 49] impedes the scheduler from using a microarray to prognose and predict the outcome of cancer. We combine GMM and KDE methods to segment spotted cDNA images. The GKDE was expected to fine tune the GMM and to determine a suitable cutting point for clustering foreground and background using the KDE. The GKDE, KDE and GMM methods can improve the reproducibility in duplicated spots, in swapped arrays and the spike gene spots. This will be useful for the advanced utilization of microarrays in biology and medicine.

In this study, the GKDE, KDE and GMM were applied to segment cDNA microarray images and the evaluation of performances was conducted. First, the spike

genes with known contents were designed on real microarrays, the criteria of SSRE and SSE measure the accuracy and performance. The GKDE, KDE and GMM more accurately estimate the features of spots than the adaptive region growing segmentation method in GenePix 6.0 does. Secondly, duplicated spots are utilized to examine expression variation on a microarray image. The KDE also has a better average relative performance, as measured by the concordance correlation coefficients, Pearson's correlation coefficients and standard deviations of expression values of duplicated spots. Finally, swapped microarray experiments were conducted to study the variation among dyes. The correlation coefficients measure the linear relationship for the selected spots with significantly differentially expressed levels. Again, the KDE is more accurate, when tested on eight pairs of real swapped cDNA microarray images.



Sixteen real microarray cDNA images were used to determine the accuracy and performance, by comparison with the adaptive irregular segmentation method in GenePix 6.0. The ratio of means is used to estimate features in segmented spots. Other statistics could be studied. Other methods for segmenting images can be studied further [50-52].

The GKDE, KDE and GMM programs were run in under one thousand seconds to test one real cDNA microarray image on a personal computer with Intel CPU 2.6 GHz

and 2GB RAM. Especially, the KDE algorithm has model free, computational efficiency and improved performance for segmenting cDNA microarray images used for biology and medicine. The method of GKDE also have similar advantages.



6. Future Works

The fully 3D reconstruction algorithms for microPET could be developed in the future. The PDEM is basically used to reconstruct 2D images now. The PDEM can not be applied to reconstruct fully 3D microPET images due to the difficulty of computing and calculus transmission probability matrix for 3D microPET data, $P(b,d)$. Once new methods are developed to solve the problem of computing $P(b,d)$, the PDEM is expected to reconstruct 3D microPET images more accurately in the future. This method can also be utilized in future works to reconstruct clinical PET images based on the same physical principle of data acquisition and mathematical models.

Meanwhile, attenuation, normalization, scattering, and partial volume effects corrections can be considered to reconstruct microPET images. It is expected that the more useful correction or normalization methods added to reconstruction algorithms will yield more accurate and less noise images in the future.

The stopping criterion of the EM algorithm can be also studied in the future. We can consider K-fold cross-validation and other possible methods. That is, the iteration will stop when the minimum predicted sum of square is reached by cross-validation. This can provide an objective method to decide the stopping criterion from data automatically. Because the EM algorithm has slow convergence rates, different methods have been proposed in literature to accelerate the EM algorithm [53]. Hence,

we can further evaluate improvements of the EM algorithm in future studies. For instance, we can consider the lazy EM algorithm [54], parallel EM algorithm [55], and related methods [56-57].

We have proposed new segmentation methods by the GMM with the KDE to improve the segmentation of 3D microPET and spotted microarray images. Automatic search of the number of clusters and initialized values can be determined by the KDE. Alternative methods for the searching of the number of clusters and initialized values from data can be investigated in the future.

Spatial information can be integrated to improve segmentation. For instance, we can select connected regions for foreground to remove isolated pixels. Other methods for segmentation of images can be further investigated and compared in future studies.



7. Acknowledgements

We thank Prof. Jyh-Cheng Chen in National Yang-Ming University, Dr. Ren-Shyan Liu and Mr. Guang-Hong Lin in Taipei Veterans General Hospital, Dr. Meei-Ling Jan in Institute of Nuclear Energy Research, Dr. Yun-Shien Lee in Chang-Gung Memorial Hospital, and their laboratories for the collaborations in providing the experimental materials, the images for microPET, and spotted microarrays in the studies.



8. References

- [1] Cunningham VJ, Jones T. Spectral analysis of dynamic PET studies. *J. Cereb. Blood Flow Metab.*, 1993, 13, 15-23.
- [2] Johnson CA, Seidel J, Carson RE, Gandler WR, Sofer A, Green MV, Daube-Witherspoon ME. Evaluation of 3D reconstruction algorithms for a small animal PET camera. *IEEE Trans. Nucl. Sci.*, 1997, 44, 1303-1308.
- [3] Chatziioannou A, Qi J, Moore A, Annala A, Nguyen K, Leahy R, Cherry SR. Comparison of 3-D maximum *a posteriori* and filtered backprojection algorithms for high-resolution animal imaging with microPET. *IEEE Trans. Med. Imag.*, 2000; 19, 507-512.
- [4] Azriel Rosenfeld, Avinash C. Kak. *Digital Picture Processing 2nd*, 1, 1982, 354.
- [5] Hudson HM, Larkin RS. Accelerated image reconstruction using ordered subsets of projection data. *IEEE Trans. Med. Imag.*, 1994, 13, 601-609.
- [6] Michel Defrise, Kinahan PE, Townsend DW, Michel C, Sibomana M, Newport DF. Exact and Approximate Rebinning Algorithms for 3-D PET Data. *IEEE Trans. Med. Imag.*, 1997, 16, 145-158.
- [7] Shepp LA, Vardi Y. Maximum likelihood reconstruction for emission tomography. *IEEE Trans. Med. Imag.*, 1982, MI-1, 113-122.

- [8] Lange K, Carson RE. EM reconstruction algorithms for emission and transmission tomography. *J. Comput. Assist. Tomogr.*, 1984, 8, 306–316.
- [9] Vardi Y, Shepp LA, Kaufman L. A statistical model for positron emission tomography. *Journal of the American Statistics Association*; 1985, 80, 8-20.
- [10] Chen CM, Lee SY, Cho ZH. Parallelization of the EM algorithm for 3D PET image reconstruction. *IEEE Trans. Med. Imag.*, 1991, 10, 513-522.
- [11] Hoffman EJ, Huang SC, Phelps ME, Kuhl DE. Quantization in positron emission computed tomography: 4. Effect of accidental coincidences. *J. Comput. Assist. Tomography*, 1981, 5, 391-400.
- [12] Casey ME, Hoffman EJ. Quantization in positron emission computed tomography: 7. a technique to reduce noise in accidental coincidence measurements and coincidence efficiency calibration. *J. Comput. Assist. Tomography*, 1986, 10, 845-850.
- [13] Rokitta O, Casey M, Wienhard K, Pietrzyk U. Random correction for positron emission tomography using singles count rates. *IEEE Nuclear Science Symposium Conference Record*, 2000, 3, 1737-1740.
- [14] Polite DG, Snyder DL. Corrections for accidental coincidences and attenuation in maximum-likelihood image reconstruction for positron-emission tomography. *IEEE Trans. Med. Imag.*, 1991, 10, 82-89.

- [15] Fessler JA, Clinthorne NH, Rogers WL. On complete-data spaces for PET reconstruction algorithms. *IEEE Trans. Nucl. Sci.*;1993, 40, 1055-1061.
- [16] Lu HHS, Tseng WJ. On accelerated cross-reference maximum likelihood estimates for positron emission tomography. *Conference Record of 1997 IEEE Nuclear Science Symposium*, 1997, 2, 1484-1488.
- [17] Lu HHS, Chen CM, Yang IH. Cross-reference weighted least square Estimates for positron emission tomography. *IEEE Trans. Med. Imag.*, 1998, 17, 1-8.
- [18] Chen JC, Liu RS, Tu KY, Lu HHS, Chen TB, Chou KL. Iterative image reconstruction with random correction for PET studies. *Proceedings of the Society of Photo-Optical Instrumentation Engineers*, 2000, 3979, 1218-1229.
- [19] Brasse D, Kinahan PE, Lartizien C, Comtat C. Correction methods for random coincidences in 3D whole body PET imaging. *IEEE Nuclear Science Symposium and Medical Imaging Conference, San Diego, CA*, 2001, 4, 2080-2084.
- [20] Yavuz M, Fessler JA. New statistical models for random pre-corrected PET scans. *Information Processing in Medical Imaging*, (Lecture Notes in Computer Science), J. Duncan and G. Gindi, Eds. Springer-Verlag, 1997, 1230, 190–203.
- [21] Ollinger JM, Fessler JA. Positron-emission tomography. *IEEE Signal Processing Magazine*, 1997, 41, 1, 43-55.

- [22] Chen JC, Tu KY, Lu HHS, Chen TB, Chou KL, Liu RS. Statistical Image Reconstruction for PET Studies. *The Biomedical Engineering Society 1998 Annual Symposium*, 1998, 71-72.
- [23] Tu KY, Chen JC, Lu HHS, Chen TB, Chou KL, Liu RS. Random Correction Using Iterative Reconstruction for PET. *European Association of Nuclear Medicine Annual Congress*, 2000.
- [24] Tu KY, Chen TB, Lu HHS, Liu RS, Chen KL, Chen CM, Chen JC. Empirical Studies of Cross-Reference Maximum Likelihood Estimate Reconstruction for Positron Emission Tomography. *Biomed. Eng. Appl. Basis Comm.*, 2001, 13, 1, 1-7.
- [25] Akaike H. A new look at the statistical model identification. *IEEE Trans. Automat. Ontr.*, 1974, AC-19, 716-723.
- [26] Wong KP, Feng D, Meikle SR, Fulham MJ. Simultaneous estimation of physiological parameters and input function: In vivo PET data. *IEEE Trans. Inform. Technol. Biomed.*, 2001, 5, 67-76.
- [27] Wong KP, Feng D, Meikle SR, Fulham MJ. Segmentation of Dynamic PET Images Using Cluster Analysis. *IEEE Transactions on Nuclear Science*, 2002, 49, 1.

- [28] McLachlan GJ, Basford KE. Mixture Models. *Inference and Applications to Clustering*. Dekker, 1988.
- [29] Hsiao IT, Rangarajan A, Gindi G. Joint-Map Reconstruction/Segmentation for transmission Tomography Using Mixture-Model as Priors. *Proc. IEEE Nuclear Science Symposium and Medical Image Conference*, 1998, 3, 1689-1693.
- [30] Dempster AP, Laird NM, Rubin DB. Maximum likelihood from incomplete data via the EM algorithm (with discussion). *J. R. Statist. Soc. B*, 1977, 39, 1-38.
- [31] Wu CFJ. On the convergence properties of the EM algorithm. *Annals of Statistics*, 1983, 11, 95-103.
- [32] Demirkaya O, Asyali MH, Shoukri MM. Segmentation of cDNA microarray spots using Markov random field modeling. *Bioinformatics*, 2005, 21 13, 2994–3000.
- [33] Yang YH, Speed TP. Design issues for cDNA microarray experiments. *Nature Reviews Genetics*, 2002, 3, 579-588.
- [34] Yang YH, Buckley MJ, Dudoit S, Speed TP. Comparison of methods for image analysis on cDNA microarray data. *Journal of Computational and Graphical Statistics*, 2002, 11, 108-136.

- [35] Li L, Lu HHS. Explore biological pathways from noisy array data by directed acyclic boolean networks. *Journal of Computational Biology*, 2005,12,2, 170-185.
- [36] Chen Y, Dougherty ER, Bittner ML. Ratio based decisions and the quantitative analysis of cDNA microarray images. *Journal of Biomedical Optics*, 1997, 2, 364-374.
- [37] Ho J, Hwang WL, Lu HHS, Lee DT. Gridding spot centers of smoothly distorted microarray images. *IEEE Transactions on Image Processing*, 2006, 15, 2, 342-354.
- [38] Yang F, Jiang T. Pixon-based image segmentation with Markov random fields. *IEEE Transactions on Image Processing*, 2003, 12, 12, 1552-1559.
- [39] Wang X, Wang H. Markov random field modeled range image segmentation. *Pattern Recognition Letters*, 2005, 25, 367-375.
- [40] Blekas K, Galatsanos NP, Likas A, Lagaris IE. Mixture Model Analysis of DNA Microarray Images. *IEEE Trans. Med. Imag.*, 2005, 24, 7, 901-909.
- [41] Sheather SJ, Jones MC. A reliable data-based bandwidth selection method for kernel density estimation. *J. Roy. Statist. Soc. B*, 1991, 683-690.
- [42] Wang TH, Lee YS, Chen ES, Kong WH, Chen LK, Hsueh DW, Wei ML, Wang HS. Establishment of cDNA microarray analysis at the Genomic Medicine

Research Core Laboratory (GMRCL) of Chang Gung Memorial Hospital.

Chang Gung Medical Journal, 2004, 27, 4, 243-260.

[43] Chao A, Wang TH, Lee YS, Hsueh S, Chao AS, Chang TC, Kung WH, Huang SL, Chao FY, Wei ML et al. Molecular characterization of adenocarcinoma and squamous carcinoma of the uterine cervix using microarray analysis of gene expression. *Int J Cancer*, 2006, 119, 191-198.

[44] Engel J, Herrmann E, Gasser T. An iterative bandwidth selector for kernel estimation of densities and their derivatives. *Journal of Nonparametric Statistics*, 1994, 4, 21-34.

[45] McLachlan GJ, Bean RW, Peel D. A mixture model-based approach to the clustering of microarray expression data. *Bioinformatics*, 2000, 18, 3: 413-22.

[46] Lin L. I-K. A Concordance Correlation Coefficient to Evaluate Reproducibility. *Biometrics*, 1989, 45, 1255-1258.

[47] Reis-Filho JS, Westbury C, Pierga JY. The impact of expression profiling on prognostic and predictive testing in breast cancer. *J. Clin. Pathol*, 2006, 59, 225-231.

[48] Sherlock G. Of fish and chips. *Nat Methods*, 2005, 2, 5, 329-330.

[49] Irizarry RA, Warren D, Spencer F, et al. Multiple-laboratory comparison of microarray platforms. *Nat Methods*, 2005, 2, 5, 345-350.

- [50] Chen CM, Lu HHS, Lin YC. An early vision based snake model for ultrasound image segmentation. *Ultrasound in Medicine and Biology*, 2000, 26, 2, 273-285.
- [51] Chen CM, Lu HHS, Huang YS. Cell-based dual snake model: A new approach to extracting highly winding boundaries in the ultrasound images. *Ultrasound in Medicine and Biology*, 2003, 28, 8, 1061-1073.
- [52] Wu HM, Lu HHS. Supervised motion segmentation by spatial-frequential analysis and dynamic sliced inverse regression. *Statistica Sinica*, 2004, 14, 413-430. C.
- [53] Liu C, Rubin DB. Maximum likelihood estimation of factor analysis using the ECME algorithm with complete and incomplete data. *Statistica Sinica*, 1998, 8, 729-747.
- [54] Thiesson B, Meek C, Heckerman D. Accelerating EM for large database, *Microsoft Research, Technical Report, MSR-TR-99-31*.
- [55] Chen CM, Lee SY, Cho ZH. Parallelization of the EM algorithm for 3D PET image reconstruction. *IEEE Trans. Med. Imag.*, 1991, 10, 513-522.
- [56] Feesler JA, Hero AO. Space-alternating generalized expectation maximization algorithm, *IEEE Trans. Signal Proc.*, 1994, 42, 569-587.
- [57] Browne J, De Pierro AR. A row-action alternative to the EM algorithm for maximizing likelihoods in emission tomography, *IEEE Trans. Med. Imag.*, 1996, 15, 687-699.

9. Appendix

A: PDEM Algorithm

The observed data of prompt and delay sinograms are assumed to follow two independent Poisson distributions in (A1) and (A2),

$$n_p^*(d) \sim \text{Poisson}(\lambda^*(d)), \quad (\text{A1})$$

$$n_d^*(d) \sim \text{Poisson}(\lambda_r^*(d)), \quad (\text{A2})$$

where $\lambda^*(d) = \lambda_t^*(d) + \lambda_r^*(d) = \sum_b P(b,d)\lambda_t(b) + \lambda_r^*(d)$, $b=1,2,\dots,B$, and $d=1,2,\dots,D$.

Then, the incomplete log-likelihood of the prompt and delay sinograms are as follows,

$$l_{in}(\lambda_t(b), \lambda_r^*(d)) = \sum_{d=1}^D \left\{ -2\lambda_r^*(d) - \sum_{b=1}^B P(b,d)\lambda_t(b) + n_p^*(d) \ln(\lambda_r^*(d)) + \sum_{b=1}^B P(b,d)\lambda_t(b) + n_d^*(d) \ln(\lambda_r^*(d)) \right\}. \quad (\text{A3})$$

Firstly, the observed data, $n_p^*(d)$ and $n_d^*(d)$, are treated as incomplete data. One possible model of complete data for the EM algorithm is given by (A4) and (A5):

$$n_p^*(b,d) \sim \text{Poisson}(p(b,d)\lambda_t(b)), \quad (\text{A4})$$

$$n_d^*(d) \sim \text{Poisson}(\lambda_r^*(d)), \quad (\text{A5})$$

where $n_p^*(b,d)$ is the number of emissions at the b^{th} pixel detected by the d^{th} tube;

$n_d^*(d)$ is the number of random (or accidental) coincidence events detected by the d^{th}

tube in the delay window; $n_p^*(b,d)$ and $n_d^*(d)$ are assumed to be statistically

independent; $n_p^*(d) = \sum_{b=1}^B n_p^*(b,d) + n_d^*(d)$. According to models (A4) and (A5), the

log-likelihood function of complete data is

$$\begin{aligned}
& L(\lambda_t(b), \lambda_r^*(d)) \\
&= \sum_d \sum_b \{n_p^*(b, d) \ln(P(b, d)\lambda_t(b)) - P(b, d)\lambda_t(b)\} \\
&+ \sum_d \{n_d^*(d) \ln(\lambda_r^*(d)) - \lambda_r^*(d)\}.
\end{aligned} \tag{A6}$$

The E-step computes the conditional expectation of the log-likelihood of complete data, given the observed incomplete data and old parameter values. In this study, λ_t^0 is initialized by the FBP and λ_r^{*0} is initialized by the method of moments, $\bar{n}_d^* = \sum_d n_d^*(d) / D$. This E-step will generate a function of new parameter values of λ_t^i and λ_r^{*i} , where i is the number of iterations, and the formula is given in (A7):

$$Q(\lambda_t^i(b), \lambda_r^{*i}(d) | \lambda_t^{i-1}(b), \lambda_r^{*i-1}(d)) = E[L(\lambda_t^i(b), \lambda_r^{*i}(d)) | n_p^*, n_d^*, \lambda_t^{i-1}(b), \lambda_r^{*i-1}(d)]. \tag{A7}$$

The M-step determines the λ_t^i and λ_r^{*i} values that maximize (A7) which can be achieved by setting the first derivatives to zero. This step will yield the solutions given in (A8) and (A9):

$$\lambda_t^i(b) = \frac{\lambda_t^{i-1}(b)}{\sum_{d=1}^D P(b, d)} \frac{\sum_{d=1}^D n_p^*(d) p(b, d)}{\sum_{b'=1}^B p(b', d) \lambda_t^{i-1}(b') + \lambda_r^{*i-1}(d)}, \tag{A8}$$

$$\lambda_r^{*i}(d) = \frac{1}{2} \left[\frac{n_p^*(d) \lambda_r^{*i-1}(d)}{\sum_{b'=1}^B p(b', d) \lambda_t^{i-1}(b') + \lambda_r^{*i-1}(d)} + n_d^*(d) \right]. \tag{A9}$$

B: Terminology

1. **Concordance correlation coefficient** (ρ_c) is used to detect the departure to 45° line.
2. **Filtered back-projection** (FBP) is an algorithm that is commonly used in transmission tomography.
3. **Full width at half-maximum** (FWHM) is a simple and well-defined measurement that is used to evaluate the quality of images obtained under different collection environments (as shown in Fig. B-1).

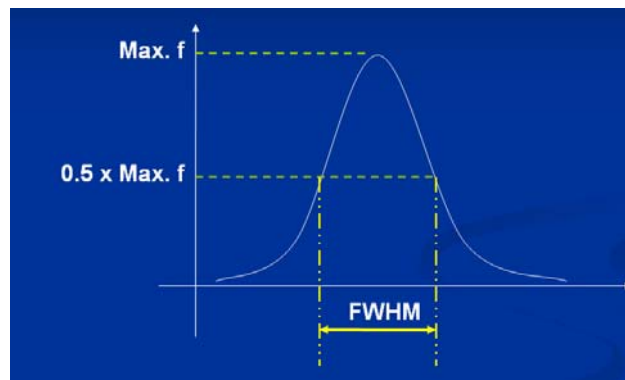


Fig. B-1: The illustration of HWHM is shown.

4. **True, random and scatter coincidence events:**

True events are two gamma rays detected within a specific time window by the PET scanner (in Fig. B-2).

Random events are two different single rays detected within a specific time window by the PET scanner (in Fig. B-2).

Scatter events are caused by two gamma rays deflected before reaching the detectors but detected within a specific time window by the PET scanner (in Fig. B-2).

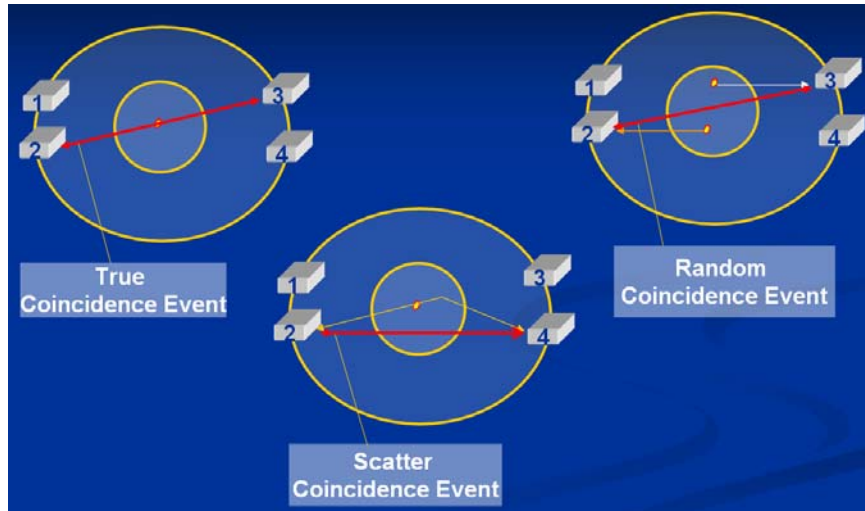


Fig. B-2: The true, random, and scatter coincidence events are illustrated.

5. Span

Span specifies how many adjacent LORs should be grouped together into the same axial angle (theta), where theta is defined to be the angle between the axial and transaxial axes. Choosing a larger span will not “throw away” data, but will reduce the size of the sinogram since there are fewer theta angles in the final sinogram. Of course, this comes at the price of degrading the axial resolution. The minimum span is 3 and the maximum is 63.

6. Ring difference

Ring difference specifies how many crystal rings away the rebinning algorithm should look for a coincidence event. For example, microPET® systems have 32

crystal rings, and therefore the maximum ring difference is 31, and if we specify a ring difference of 31, this means that coincidences that occur between crystal ring 1 and crystal ring 32 (ring difference = $32 - 1$) will be included in the sinogram, as well as all possible combinations of crystal rings. A ring difference of 3 means that coincidences between crystal ring 16 and crystal rings 13, 14, 15, 16, 17, 18 and 19 will be included, but not coincidences between crystal rings 16 and 12, for example. The minimum allowed ring difference is 1 resulting in a reconstructed image always containing 63 planes instead of 32 (a ring difference of 0 would be needed to only have 32 planes). Not using the maximum allowed ring difference means that not all of the data will be used (i.e. data will be “thrown” away).

